

# Scale-variant Topological Information for Characterizing Complex Networks

Quoc Hoan Tran<sup>\*1</sup>, Van Tuan Vo<sup>\*1</sup>, and Yoshihiko Hasegawa<sup>†1</sup>

<sup>1</sup> *Department of Information and Communication Engineering  
Graduate School of Information Science and Technology  
The University of Tokyo, Tokyo 113-8656, Japan  
{zoro\*,tuan\*,hasegawa†}@biom.t.u-tokyo.ac.jp*

December 15, 2024

## Abstract

Real-world networks are difficult to characterize because of the variation of topological scales, the non-dyadic complex interactions and the fluctuations. Here, we propose a general framework to address these problems via a methodology grounded on topology data analysis. By observing the diffusion process in a network at a single specified timescale, we can map the network nodes to a point cloud, which contains the topological information of the network at a single scale. We then calculate the point clouds constructed over variable timescales, which provide scale-variant topological information and enable a deep understanding of the network structure and functionality. Experiments on synthetic and real-world data demonstrate the effectiveness of our framework in identifying network models, classifying real-world networks and detecting transition points in time-evolving networks. Our work presents a unified analysis that is potentially applicable to more complicated network structures such as multilayer and multiplex networks.

Characterizing the structure of complex networks is the most fundamental issue in deciphering network dynamics. The network anatomy is quite relevant to phenomena occurring in networks such as spread of information or epidemic disease or robustness and stability under attack. A considerable number of applications have been of great interest in the literature. These applications include controlling and predicting patterns of dynamics in networks<sup>1-3</sup>, quantifying structural and functional similarities of biological networks<sup>4-6</sup> and detecting transition points in time-evolving networks<sup>7-9</sup>.

In practice, the structure of real-world networks is inherently difficult to characterize. First, real-world networks have complex patterns that are reflected at various topological scales<sup>10-12</sup> (Fig. 1a). In revealing these patterns, the conventional statistical measures<sup>13,14</sup> and methods<sup>10,15-18</sup> remain ill-defined as evidenced by the lack of representation of the variation of topological scales. Second, real-world networks are representations of complex systems that have dyadic and non-dyadic interactions<sup>19-21</sup> (Fig. 1b). However, the majority of the current methods for characterizing complex networks focus only on the dyadic interactions between nodes such as detecting the existence of pairwise edges or paths connected by successive edges. Third, real-world networks often suffer from fluctuation caused by external factors<sup>22</sup>. Because of the fluctuation, the quest for unifying the principles underlying the topology of networks emerges only in simple idealized models without any additional effect<sup>23-25</sup>. Robust representations under the fluctuation have not been explored for characterizing structures of real-world networks.

Our main goal is to propose a general framework for addressing the abovementioned problems. To reveal the variation of topological scales, we rely on the obtained topological information along with the diffusion process exhibited in the network. When the diffused time  $\tau$  is small, the microscale structure is revealed as there is almost no information exchanged between the nodes. Increasing  $\tau$  will reflect the mesoscale decomposition of the network until the macroscale structure is finally captured. At each  $\tau$ , we map the network nodes to a point cloud, where a group of close points represents the unit of points that easily exchange information in the diffusion process. To capture the non-dyadic interactions, we construct a simplicial complex model<sup>26</sup> from the point cloud. To obtain a robust representation, we use the topological data analysis<sup>26-29</sup>, which is a set of computational topology methods, to encode the simplicial complex model into noise-tolerant quantitative features. Observing these features with varying  $\tau$  provides insights into the variation of topological scales as well as the interplay between the structure

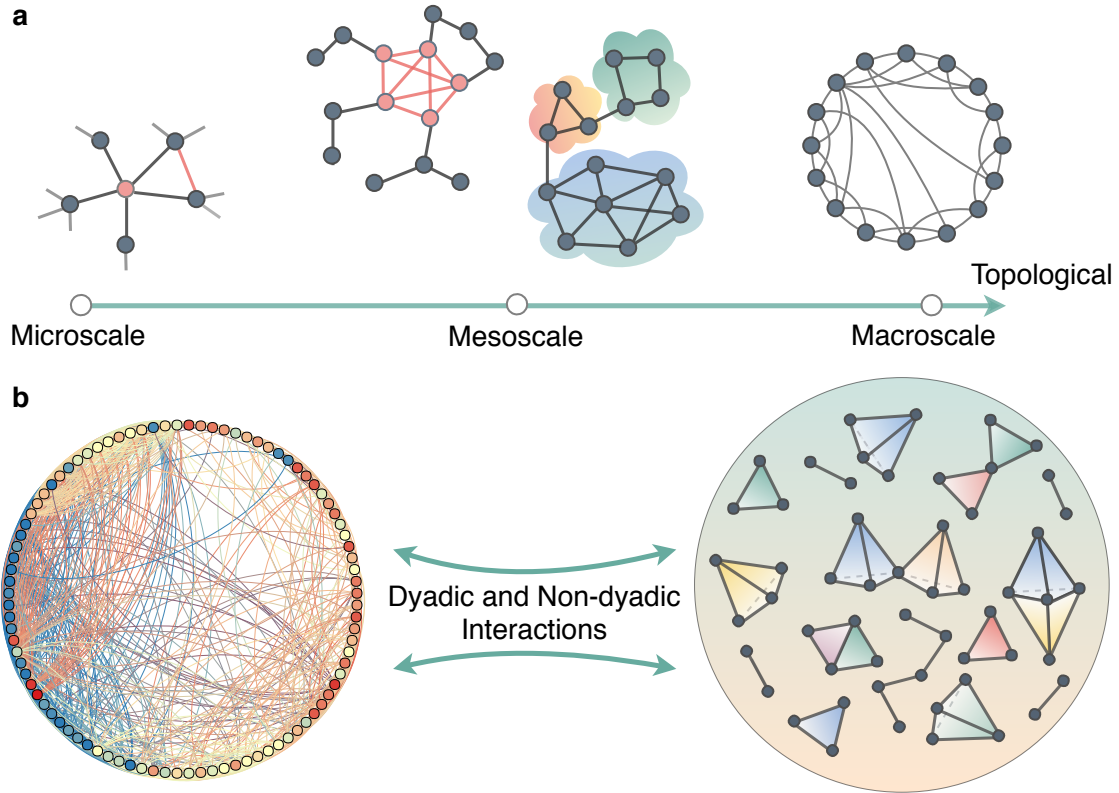


**Figure 1 | Various topological scales and interactions between multiple elements in a complex network.** (a) Complex networks can be analysed at various topological scales ranging from individual nodes (microscale) to whole networks (macroscale). In between the two scales, there is mesoscale, where we can observe patterns of collectives, cores and peripheries. (b) Complex network is a representation of a complex system having dyadic and non-dyadic interactions between its elements. The interactions can be represented as simplices such as segments (for dyadic interactions), filled triangles or filled tetrahedrons (for non-dyadic interactions involving three or four elements) and so on.

and dynamics of the network. Therefore, we construct scale-variant topological features by regarding  $\tau$  as a variable parameter rather than as a single fixed value.

The proposed framework allows us to study the properties of complex networks that might reflect the variation of topological scales, provide in-depth understanding of the complex interactions and evaluate the robustness under the fluctuation. By analysing several network models, we demonstrate that our framework can characterize the parameters that are used to generate the networks. Interestingly, using the scale-variant topological features, we can distinguish networks generated from different models with empirically better results than other conventional approaches. We further apply our framework to classify real-world networks and detect the transition points in time-evolving gene regulatory networks. We believe that our study can provide a unified analysis of complex networks. Such a study has the potential to enable further applications to more complex network structures such as multilayer and multiplex networks.

## Results

### Scale-variant topological features

We consider an undirected weighted network  $\mathcal{G}$  with  $N$  nodes  $v_1, \dots, v_N$ . We suppose that there is a single random walker, which moves randomly between nodes in continuous time. When the walker is located at  $v_i$ , we assume that the walker moves to the neighbour node  $v_j$  with the transition rate  $w_{ij}/k_i$ , where  $w_{ij} \geq 0$  represents the weight of the edge from  $v_i$  to  $v_j$  ( $i, j \in \{1, 2, \dots, N\}$ ) and  $k_i = \sum_{j=1}^N w_{ij}$ . Here,  $w_{ij} = 0$  if there is no edge between  $v_i$  and  $v_j$ . We denote  $p_{\mathcal{G},k}(\tau|i)$  as the probability of finding

a random walker on  $v_k$  at time  $\tau$  that starts from  $v_i$ . The probability distribution vector  $\mathbf{p}_{\mathcal{G}}(\tau|i) = [p_{\mathcal{G},1}(\tau|i), \dots, p_{\mathcal{G},N}(\tau|i)]$ , is given according to the solution of the Kolmogorov forward equation:

$$\frac{d\mathbf{p}_{\mathcal{G}}(\tau|i)}{dt} = -\mathbf{p}_{\mathcal{G}}(\tau|i)\mathbf{L}_{\mathcal{G}}^{\text{rw}}. \quad (1)$$

Here,  $\mathbf{L}_{\mathcal{G}}^{\text{rw}}$  is the random walk Laplacian whose components  $l_{ij}$  ( $i, j \in \{1, 2, \dots, N\}$ ) are given as

$$l_{ij} = \begin{cases} 1 & \text{if } i = j \text{ and } k_i \neq 0 \\ -1/k_i & \text{if } i \neq j \text{ and } v_i \text{ is adjacent to } v_j \\ 0 & \text{otherwise.} \end{cases} \quad (2)$$

At a specific  $\tau$ , we map the nodes of network  $\mathcal{G}$  to a point cloud of  $N$  points  $\mathbf{p}_{\mathcal{G}}(\tau|1), \dots, \mathbf{p}_{\mathcal{G}}(\tau|N)$ . The shape of this point cloud offers valuable insights into the information exchange process at time  $\tau$  and the structural property of network  $\mathcal{G}$  at  $\tau$ -scale. As illustrated in Fig. 2a, we consider an undirected network comprising of four clusters, in which there are more intra-cluster connections than inter-cluster connections. At each  $\tau$ , the pairwise distances of the mapped points of the nodes in the same clusters are smaller than the distances between the nodes belonging to different clusters. These distances decrease as we increase  $\tau$ . Consequently, the hole patterns in the point cloud appear with different sizes in different groups of points when  $\tau$  varies (Fig. 2b). Observing the formation of these holes while varying  $\tau$  can reveal the variation of topological scales for the network.

To capture the non-dyadic interactions at each  $\tau$ -scale, we construct the Vietoris–Rips simplicial complex<sup>26,30</sup>, which is a set of simplices built with a non-negative threshold  $\varepsilon$ . In this simplicial complex, each simplex is built over a subset of points if all pairwise distances between the points are less than or equal to  $\varepsilon$ . With different  $\varepsilon$  values, we have different simplicial complexes and hence different topological information regarding the number, the position and the size of high-dimensional holes such as connected components, loops and tunnels. We obtain a sequence of embedded simplicial complexes called filtration with increasing  $\varepsilon$  (see Supplementary Note 1 and Supplementary Fig. 1). From the filtration, we can highlight not only the simple connectivity but also how network properties change as information propagates.

To encode the hole patterns over the filtration into the quantitative features, we consider the emergence and disappearance of these patterns as topological features for the complex network at  $\tau$ -scale. We use the persistent homology theory<sup>26–29,31</sup> to study these topological features and visualize the results through multi-set points in a two-dimensional *persistence diagram*. In this diagram, each point  $(b, d)$  represents an  $l$ -dimensional hole that appears at  $\varepsilon = b$  (known as the *birth-scale*) and disappears at  $\varepsilon = d$  (known as the *death-scale*) across the filtration (Fig. 2c). Here, the connected components are zero-dimensional, loops or tunnels are one-dimensional and voids are two-dimensional holes.

We obtain the scale-variant topological features that reflect the variation of the topological scales by considering the two-dimensional persistence diagrams when  $\tau$  varies. We denote  $Dg_{l,\tau}^{(2)}(\mathcal{G})$  as the two-dimensional persistence diagram of network  $\mathcal{G}$  calculated for  $l$ -dimensional holes at  $\tau$ -scale. We consider  $\tau$  in a pre-defined set  $\mathcal{T} = \{\tau_1, \tau_2, \dots, \tau_K\}$ , where  $0 < \tau_1 < \tau_2 < \dots < \tau_K$  (with  $K$  denoting the set's size). We define the scale-variant topological features, i.e. the three-dimensional persistence diagram of  $l$ -dimensional holes for network  $\mathcal{G}$ , as  $Dg_l^{(3)}(\mathcal{G}) = \{(b, d, \tau) \mid (b, d) \in Dg_{l,\tau}^{(2)}(\mathcal{G}), \tau \in \mathcal{T}\}$  (Fig. 2d).

To use the three-dimensional persistence diagrams for statistical-learning tasks, we use the positive-definite kernel mapping for such diagrams introduced in ref.<sup>32</sup> (see Methods for the definition of this kernel and its normalized version). We can apply this kernel to detect the transition point in the structure of a network collection  $\{\mathcal{G}_1, \mathcal{G}_2, \dots, \mathcal{G}_M\}$ . We consider a collection of diagrams  $\mathcal{D} = \{Dg_1, \dots, Dg_M\}$ , where  $Dg_i$  is a three-dimensional persistence diagram of network  $\mathcal{G}_i$ . We use the kernel Fisher discriminant ratio<sup>33</sup>  $\text{KFDR}_{M,s}(\mathcal{D})$  calculated from the Gram matrix  $(k_{ij})_{i,j=1,\dots,M}$ , where  $k_{ij}$  is the kernel value between  $Dg_i$  and  $Dg_j$ .  $\text{KFDR}_{M,s}(\mathcal{D})$  is a statistical quantity to measure the dissimilarity between two classes assumptively defined by two sets of data having index before and from  $s$  (Supplementary Note 2). Here, the index  $s$  achieving the maximum of  $\text{KFDR}_{M,s}(\mathcal{D})$  corresponds to the estimated transition point.

## Robustness of scale-variant topological features

We show that the scale-variant topological features, i.e. the three-dimensional persistence diagrams computed from a network, are robust with respect to some perturbations of the network. To formalize such robustness, we first explain the concept of *bottleneck distance*, which is a metric structure for comparing

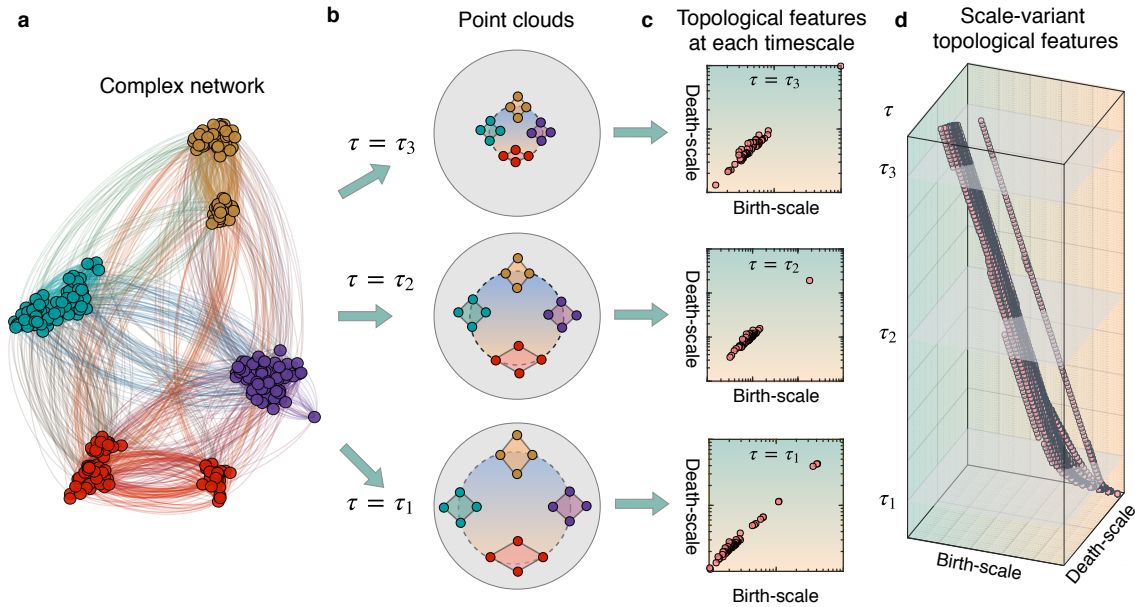


**Figure 2 | Scale-variant topological features reflecting the variation of topological scales.** (a) An undirected network comprising four clusters in which there are more connections within intra-clusters than between inter-clusters. (b) At each timescale  $\tau$ , we map the nodes to a point cloud in which the distances of the mapped points of the nodes in the same clusters are smaller than those between the nodes belonging to different clusters. These distances decrease as  $\tau$  increases as  $\tau_1 < \tau_2 < \tau_3$ . The hole patterns in the point cloud such as connected components, loops and tunnels appear with different sizes in different groups of points at varying  $\tau$ . (c) The topological features at each  $\tau$  characterize the shape of the point cloud. These features are displayed as a two-dimensional persistence diagram for the holes appeared at each  $\tau$ -scale. We illustrate here the two-dimensional persistence diagram for one-dimensional holes (loops and tunnels). The axes of the diagrams are represented at the logarithmic scale. (d) We obtain the scale-variant topological features, i.e. the three-dimensional persistence diagram, by integrating two-dimensional diagrams at varying  $\tau$ . The birth-scale and death-scale axes of the diagrams are represented at the logarithmic scale.

persistence diagrams<sup>32</sup>. Given two three-dimensional persistence diagrams  $E$  and  $F$ , consider all matchings  $\psi$  such that a point on one diagram is matched to a point on the other or to its projection on the plane  $b = d$ . For each pair  $(\mathbf{p}, \mathbf{q}) \in \psi$  for which  $\mathbf{p} = (b_1, d_1, \tau_1)$  and  $\mathbf{q} = (b_2, d_2, \tau_2)$ , we define the *relative infinity-norm distance* between  $\mathbf{p}$  and  $\mathbf{q}$  as  $d_\xi^{(\infty)}(\mathbf{p}, \mathbf{q}) = \max(|b_1 - b_2|, |d_1 - d_2|, \xi|\tau_1 - \tau_2|)$ . Here,  $\xi$  is a positive rescaling coefficient introduced to adjust the scale difference between the point-wise distance and time. The bottleneck distance,  $d_{B,\xi}^{(3)}(E, F)$ , is defined as the infimum of the longest matched relative infinity-norm distance over all matchings,  $\psi$ :

$$d_{B,\xi}^{(3)}(E, F) = \inf_{\psi} \max_{(\mathbf{p}, \mathbf{q}) \in \psi} d_\xi^{(\infty)}(\mathbf{p}, \mathbf{q}). \quad (3)$$

If two undirected networks  $\mathcal{G}$  and  $\mathcal{H}$  with the same number  $N$  of nodes are given, we show that the bottleneck distance between  $Dg_l^{(3)}(\mathcal{G})$  and  $Dg_l^{(3)}(\mathcal{H})$  is bounded from above by the matrix 2-norm of the difference between their random walk Laplacian matrices

$$d_{B,\xi}^{(3)}(Dg_l^{(3)}(\mathcal{G}), Dg_l^{(3)}(\mathcal{H})) \leq 2\tau_K \|\mathbf{L}_{\mathcal{G}}^{\text{rw}} - \mathbf{L}_{\mathcal{H}}^{\text{rw}}\|_2. \quad (4)$$

Here,  $\|\mathbf{A}\|_2$  is the matrix 2-norm of matrix  $\mathbf{A}$  induced by the Euclidean vector norm and defined as  $\|\mathbf{A}\|_2 = \max_{\|\mathbf{x}\|_2=1} \|\mathbf{A}\mathbf{x}\|_2$ . In Supplementary Note 3, we present our proof for Eq. (4), which is based on the stability properties of two-dimensional persistence diagrams<sup>34</sup> and the sensitivity of the matrix exponential<sup>35</sup>.

The inequality of Eq. 4 states the following important property. Our scale-variant topological features are robust with respect to the perturbation applied to the random walk Laplacian matrix of the network. Therefore, these features can be used as discriminative features to characterize networks.

## Understanding variations of the parameters of network models

Using network models listed below, we investigate how the scale-variant topological features reflect variations of the parameters of network models. We generate networks from Girvan–Newman<sup>36</sup> (GN), Lancichinetti–Fortunato–Radicchi<sup>37,38</sup> (LFR), Erdős–Rényi<sup>39</sup> (ER), Watts–Strogatz<sup>40</sup> (WS), Lancichinetti–Fortunato–Radicchi with hierarchical structure<sup>17</sup> (LFR–H) and Sales–Pardo<sup>16</sup> (SP) models (see Methods for the description). We focus on the model parameters that represent the topological scale of these networks. These parameters are the ratio  $r$  between the probability of inter-community links ( $p_{\text{out}}$ ) and intra-community links ( $p_{\text{in}}$ ) in the GN model, the mixing rate  $\mu$  in the LFR model, the rewiring probability  $\beta$  in the WS model, the pair-link probability  $p_{\text{link}}$  in the ER model, the mixing rate  $\mu_{\text{macro}}$  for macro-communities in the LFR–H model and  $\rho$ , which quantifies the separations between topological scales in the SP model. We generate a number of network realizations at each value of the parameters and then observe the variation in the kernel space when these parameters vary.

We compute the three-dimensional persistence diagrams for one-dimensional holes with timescale values  $\tau_1 = 1, \tau_2 = 2, \dots, \tau_{100} = 100$ . Figure 3 shows the three-dimensional projections of the principal components from the kernel space of each model, where points with different colours represent the networks generated from different values of the parameters. In ER, WS, LFR–H and SP models, the scale-variant topological features reflect the variation of the parameters associated with the topological scales because points located at different positions have different colours (Fig. 3c-f). In GN and LFR models, there are variations in the topological scales of the network as  $r$  ( $= p_{\text{out}}/p_{\text{in}}$ ) and  $\mu$  vary from 0 (four separate groups) to 1 (a purely random graph). We detect the transition point for the series of networks obtained when increasing  $r$  as  $r_1 = 0.01, r_2 = 0.02, \dots, r_{100} = 1.0$  (GN model) and  $\mu$  as  $\mu_1 = 0.01, \mu_2 = 0.02, \dots, \mu_{100} = 1.0$  (LFR model). We obtain the phase transition at  $r = 0.12$  (Supplementary Fig. 2) and  $\mu = 0.26$  (Supplementary Fig. 3). These values correspond to the boundaries between the identifiable phases, where parameters can be identified from the kernel space, and the non-identifiable phases (Fig. 3a,b).

## Identification of network models

To evaluate the effectiveness of the scale-variant topological features, we demonstrate that the features can distinguish the networks generated from different models even if they have similar global statistical measures. We focus on GN, LFR and WS models with the same parameter settings as in the previous section. In each model, we generate 10 networks for each value of the model parameter. We consider the configuration model<sup>41</sup>, which generates random networks (known as the *configuration networks*) having the same sequences of node degrees as a given network. We generate 1000 networks from the GN model

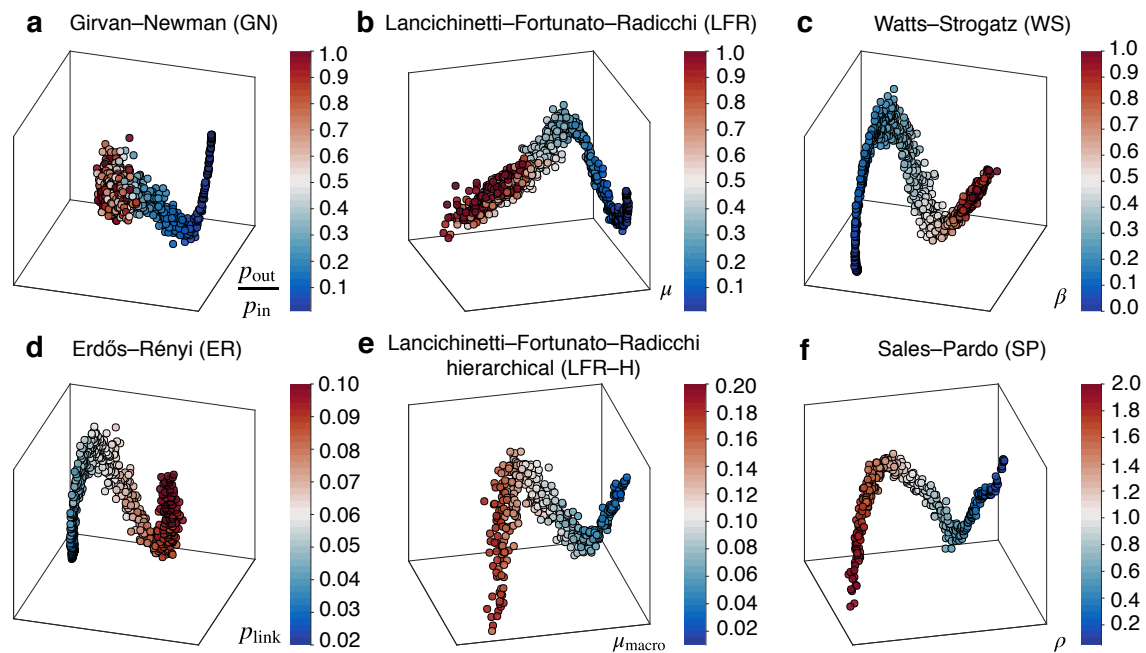


**Figure 3 | The kernel principal component projection of the scale-variant topological features for one-dimensional holes in each considered network model.** The different colours represent data generated from different values of the model parameters. We generate networks from (a) Girvan–Newman (GN), (b) Lancichinetti–Fortunato–Radicchi (LFR), (c) Watts–Strogatz (WS), (d) Erdős–Rényi, (e) Lancichinetti–Fortunato–Radicchi hierarchical (LFR–H) and (f) Sales–Pardo (SP) models. We vary the parameters for these models as  $r = p_{\text{out}}/p_{\text{in}} = 0.01, 0.02, \dots, 1.0$  (GN),  $\mu = 0.01, 0.02, \dots, 1.0$  (LFR),  $\beta = 0.00, 0.01, \dots, 1.0$  (WS),  $p_{\text{link}} = 0.020, 0.021, \dots, 0.1$  (ER) and  $\mu_{\text{macro}} = 0.01, 0.02, \dots, 0.2$  (LFR–H),  $\rho = 0.05, 0.10, \dots, 2.0$  (SP).

(GN–original), 1000 networks from the LFR model (LFR–original) and 1010 networks from the WS model (WS–original), with their corresponding configuration networks denoted as GN–config, LFR–config and WS–config, respectively. We compute the three-dimensional persistence diagrams for one-dimensional holes of these networks with timescale values  $\tau_1 = 1, \tau_2 = 2, \dots, \tau_{100} = 100$ . We calculate the kernel for these diagrams, then perform the three-dimensional projections of the principal components from the kernel space (Fig. 4a). Here, points with different colours represent the networks generated from different models. In Fig. 4a, points appear to be distinguishable by their colours.

We quantify to what extent the proposed framework identifies the networks generated from different models. We perform the scale-variant method, which uses the scale-variant topological features to classify networks into six labels as GN–original, LFR–original, WS–original, and GN–config, LFR–config and WS–config. For 10 networks generated at each value of the model parameters, we randomly split them into five networks for training and the remaining five for testing. We use the support vector machine<sup>42</sup> for classification in the normalized kernel space. Figure 4b shows the average normalized confusion matrix over 100 random splits, where the row and column labels are predicted and true labels, respectively. Using the scale-variant topological features, we can identify almost perfectly the networks that are generated from different models. Networks with GN–original, LFR–original and WS–original labels can be identified with about 99% accuracy. Interestingly, the features allow us to capture the difference between the networks and their configuration networks even if they have the same sequences of node degrees. Figure 4b shows a considerably high accuracy for GN–config (94%), LFR–config (99%) and WS–config (96%). This result indicates that the scale-variant topological features appear to reflect the essential behaviours of network models.

To highlight the benefits of the scale-variant method, we compare it with other conventional methods. These methods use the common statistical measures extracted from the network (see Methods), the graph kernels to measure the similarity between networks and the topological features calculated at a fixed topological scale. In Supplementary Note 4, we describe the graph kernels that are based on random walks (KStepRW, GeometricRW, ExponentialRW)<sup>43,44</sup>, paths (ShortestPath<sup>45</sup>), limited-sized subgraphs (Graphlet<sup>46</sup>) and subtree patterns (Weisfeiler–Lehman<sup>47</sup>). The implementations of these graph kernels can be found in ref.<sup>48</sup>. We consider two variants of topological features calculated from average distance matrix  $\Delta_{\text{avg}} = (1/K) \sum_{i=1}^K \Delta_{\tau_i}$  (scale-average), and average normalized distance matrix  $\tilde{\Delta}_{\text{avg}} = (1/K) \sum_{i=1}^K \tilde{\Delta}_{\tau_i}$  (scale-norm-average). Here,  $\Delta_{\tau_i}$  is the distance matrix of pairwise Euclidean distances between points  $\mathbf{p}_G(\tau_i|1), \dots, \mathbf{p}_G(\tau_i|N)$  (see Supplementary Note 1 and Supplementary Fig. 1), while  $\tilde{\Delta}_{\tau_i}$  is obtained by dividing  $\Delta_{\tau_i}$  by its maximum element<sup>49</sup>.

We compute the average classification accuracy over 100 random splits at different proportions of training data of 10 networks generated at each value of the model parameters. Figure 4c highlights the significant advantages of the scale-variant method. The accuracy of the scale-variant method shows notably higher values compared to the other methods. Even with a small size of the training dataset, e.g. only 10% of all data, the scale-variant method can achieve about 97% of accuracy. In contrast, the accuracies of the other methods are not higher than 84%. Remarkably, the accuracy of the scale-variant method does not change over a wide range of proportions of training data. These results demonstrate the effectiveness and the reliability of using the scale-variant topological features compared to the conventional methods to capture the differences between network structures.

## Classification of real-world network data

We apply scale-variant topological features to real-world datasets of bioinformatics networks (MUTAG, BZR, COX2, DHFR, FRANKENSTEIN, PROTEINS, NCI1, NCI109) and social networks (IMDB–BINARY, IMDB–MULTI). All networks are available at ref.<sup>50</sup> (see Methods for the description). The bioinformatics datasets have discrete labels for nodes that may be useful, but we only use the connectivity information to evaluate the classification methods. We compute three-dimensional persistence diagrams with timescale values  $\tau_1 = 1, \dots, \tau_{50} = 50$  and use the sum kernel of the normalized kernel for zero-dimensional and one-dimensional holes.

We compare the scale-variant method with the methods that use the common statistical measures, the graph kernel methods and the scale-average and scale-norm-average methods described in the previous section. Table 1 presents the average accuracies along with their standard deviations over 100 train-test splits. For each split of each dataset, we randomly take 80% of the networks for training and the remaining 20% for testing. In Table 1, the best and the second-best average accuracy scores for each dataset are coloured dark pink and light pink, respectively. The scale-variant method outperforms all the other methods on average. For seven out of 10 datasets, it offers the best results and the second-best

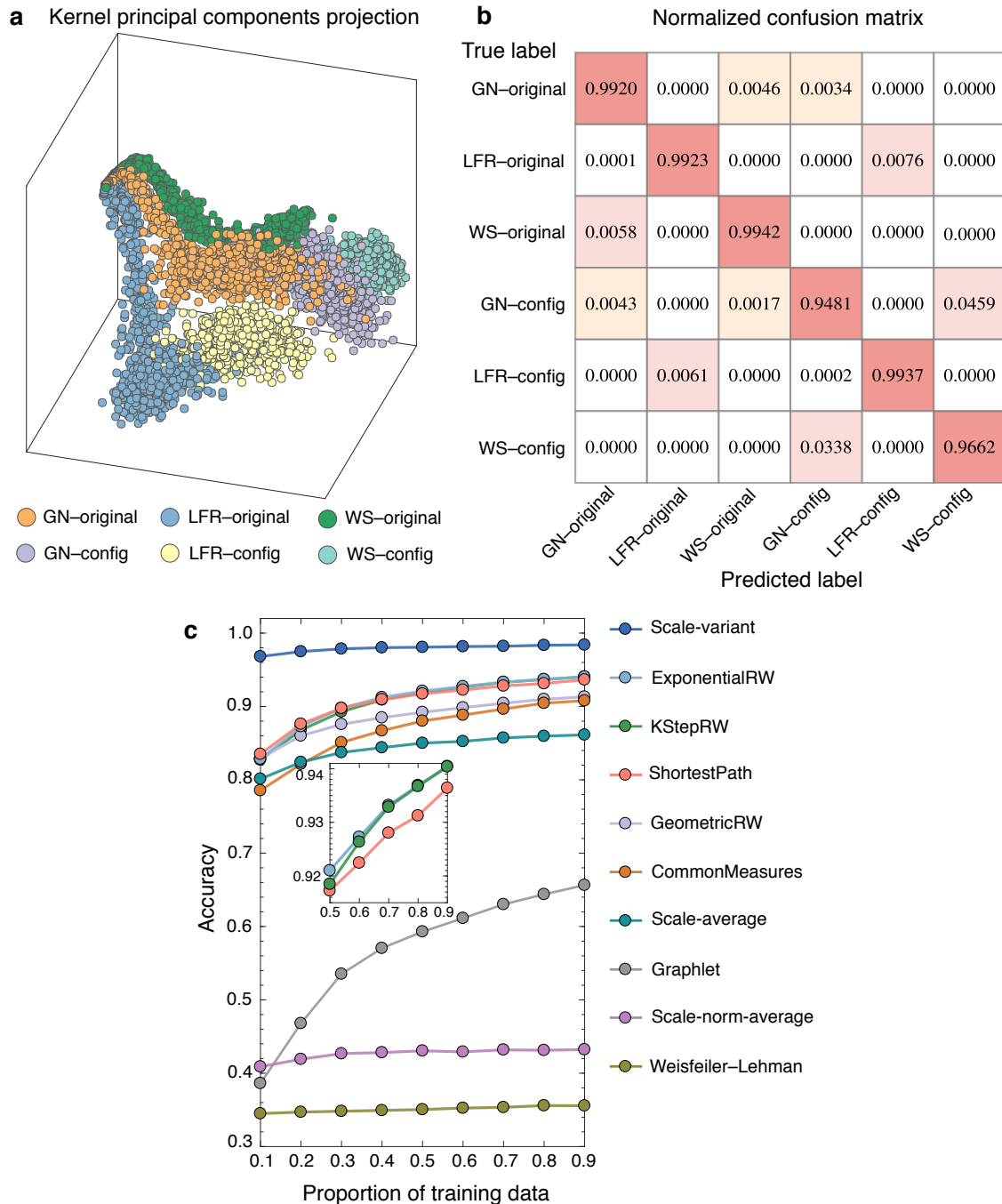


**Figure 4 | Scale-variant topological features applied to classify networks generated from different models.** We generate 1000 networks from the GN model, 1000 networks from the LFR model and 1010 networks from the WS model, with labels as GN-original, LFR-original and WS-original, respectively. We generate their corresponding configuration networks with labels as GN-config, LFR-config and WS-config, respectively. Using the scale-variant topological features, we perform the scale-variant method to classify total 6020 networks into these six labels. **(a)** The kernel principal component projection of the scale-variant topological features for these networks. The different colours represent the networks generated from different models. **(b)** The normalized confusion matrix of the scale-variant method over 100 random train-test splits of the data. For 10 networks generated at each value of the model parameters, we randomly split them into five networks for training and the remaining five for testing. **(c)** Comparison of the classification methods based on their average accuracies over 100 random train-test splits at each different proportion of the training data. The inset highlights the accuracies of the ExponentialRW, KStepRW and ShortestPath methods when the proportion of the training data varies from 0.5 to 0.9.



**Table 1** | The average and standard deviation (mean $\pm$ sd) of the classification accuracy (%) for datasets MUTAG, BZR, COX2, DHFR, FRANKENSTEIN, PROTEINS, NCI1, NCI109, IMDB-BINARY and IMDB-MULTI. In each dataset, the best and the second-best scores are coloured in dark pink and light pink, respectively.

Method	MUTAG	BZR	COX2	DHFR	FRANKENSTEIN	PROTEINS	NCI1	NCI109	IMDB-BINARY	IMDB-MULTI
Scale-variant	88.3 $\pm$ 5.1	86.8 $\pm$ 3.0	78.4 $\pm$ 1.8	78.4 $\pm$ 2.9	69.4 $\pm$ 1.5	72.6 $\pm$ 2.0	71.6 $\pm$ 1.3	70.5 $\pm$ 1.2	72.9 $\pm$ 3.0	50.3 $\pm$ 2.5
Graphlet	83.4 $\pm$ 5.7	78.2 $\pm$ 0.4	77.7 $\pm$ 0.0	61.2 $\pm$ 0.0	57.0 $\pm$ 0.7	71.8 $\pm$ 2.1	62.9 $\pm$ 1.5	62.8 $\pm$ 1.4	59.0 $\pm$ 3.5	41.0 $\pm$ 2.2
KStepRW	82.7 $\pm$ 5.8	85.6 $\pm$ 3.1	76.9 $\pm$ 2.0	75.7 $\pm$ 3.1	69.1 $\pm$ 1.4	73.4 $\pm$ 2.4	67.6 $\pm$ 1.5	68.1 $\pm$ 1.6	61.0 $\pm$ 3.6	45.6 $\pm$ 2.5
GeometricRW	82.8 $\pm$ 5.9	84.7 $\pm$ 3.2	77.1 $\pm$ 1.9	75.4 $\pm$ 3.0	68.8 $\pm$ 1.4	72.1 $\pm$ 2.2	65.6 $\pm$ 1.5	65.5 $\pm$ 1.5	67.5 $\pm$ 3.6	47.9 $\pm$ 2.7
ExponentialRW	82.9 $\pm$ 5.8	86.2 $\pm$ 3.2	76.9 $\pm$ 2.0	75.9 $\pm$ 3.3	68.7 $\pm$ 1.4	72.3 $\pm$ 2.3	65.4 $\pm$ 1.5	65.7 $\pm$ 1.6	66.4 $\pm$ 3.3	47.4 $\pm$ 2.6
ShortestPath	82.1 $\pm$ 6.1	84.6 $\pm$ 3.1	77.1 $\pm$ 1.7	74.7 $\pm$ 3.4	66.3 $\pm$ 1.5	72.4 $\pm$ 2.2	64.9 $\pm$ 1.5	64.7 $\pm$ 1.4	58.0 $\pm$ 3.6	43.9 $\pm$ 2.6
Weisfeiler-Lehman	85.2 $\pm$ 5.4	84.9 $\pm$ 2.8	77.4 $\pm$ 1.5	77.2 $\pm$ 3.3	71.5 $\pm$ 1.4	72.6 $\pm$ 2.2	71.0 $\pm$ 1.3	71.6 $\pm$ 1.5	61.2 $\pm$ 2.9	47.8 $\pm$ 2.3
CommonMeasures	84.7 $\pm$ 4.8	82.8 $\pm$ 1.8	77.7 $\pm$ 0.0	69.7 $\pm$ 3.0	63.7 $\pm$ 1.3	75.6 $\pm$ 2.2	67.4 $\pm$ 1.5	67.1 $\pm$ 1.4	71.6 $\pm$ 2.7	45.4 $\pm$ 2.4
Scale-average	85.9 $\pm$ 5.7	79.1 $\pm$ 1.3	77.7 $\pm$ 0.0	67.3 $\pm$ 3.1	62.7 $\pm$ 1.1	70.9 $\pm$ 1.9	66.8 $\pm$ 1.6	66.1 $\pm$ 1.6	71.0 $\pm$ 2.8	33.3 $\pm$ 0.0
Scale-norm-average	85.3 $\pm$ 6.0	81.1 $\pm$ 1.6	77.7 $\pm$ 0.0	61.2 $\pm$ 0.0	60.4 $\pm$ 1.3	71.7 $\pm$ 1.9	65.3 $\pm$ 1.8	65.6 $\pm$ 1.4	70.8 $\pm$ 2.8	46.0 $\pm$ 2.3

results for two other datasets. This result suggests that the method based on the scale-variant topological features can be considered to be an effective approach for classifying real-world network data.

## Detection of transition points in the time-evolving gene regulatory network

Using our scale-variant topological features, we detect transition points of the *Drosophila Melanogaster* gene regulatory network. We use a genome-wide microarray profiling that revealed the expression patterns of 4028 genes simultaneously measured during the development of *Drosophila Melanogaster*<sup>51</sup>. Based on ref.<sup>52</sup>, 66 time points are chosen from the full developmental cycle, i.e. the embryonic stage (time points 1–30), the larval stage (time points 31–40), the pupal state (time points 41–58) and the adulthood stage (time points 59–66). Along with ref.<sup>53</sup>, the time-evolving gene regulatory networks are constructed for 588 genes, which are known to be related to the developmental process based on their gene ontologies. For each gene regulatory network, we compute the three-dimensional persistence diagrams for one-dimensional holes with timescale values  $\tau_1 = 1, \dots, \tau_{100} = 100$ . Supplementary Fig. 4–7 depicts the three-dimensional persistence diagrams at full time points ranging from  $t = 1$  to  $t = 66$ .

We detect the transition point in a window of consecutive time points spanning between two consecutive states. In each window, we identify the transition time point  $t_c$ , which is the time index achieving the maximum value of the kernel Fisher discriminant ratio. From the embryonic stage to the larval stage (Fig. 5a), we obtain the transition time points as  $t_c = 28$  and  $t_c = 31$ , which are relatively close to the experimentally known transition time point  $t = 31$  from the profiling. From the larval stage to the pupal stage (Fig. 5b) and from the pupal stage to the adulthood stage (Fig. 5c), we obtain the transition time points as  $t_c = 41$  and  $t_c = 59$ , respectively. These points agree with the experimentally known transition time points. Our results suggest that our framework can detect transition points in dynamic time-evolving networks using the network structures alone.

## Discussion

The main goal of this study was to represent the variation of topological scales, capture the non-dyadic interactions and provide the robustness against noise in characterizing complex networks. Here, we proposed a general framework for constructing the scale-variant topological features from the diffusion process exhibited in networks. These features can be considered as discriminate features to identify the respective networks. Theoretically, we derived a strong mathematical guarantee for the robustness of these features with respect to the perturbations applied to the networks. Through several experiments, we provided empirical evidence for the effectiveness of these features in applications such as classification and transition point detection. Our results suggest that the observation of the topological features induced from the network dynamics over variant scales can characterize the structure and the functionality of networks.

The scale-variant topological features in our framework do not directly correspond to the common statistical measures that are constructed from the dyadic interactions between nodes at a single fixed topological scale. Our features rather encode the information of both dyadic and non-dyadic interactions in networks at variant topological scales. In the classification of networks, our features act as strong and essential factors to identify the networks. As an application to the time-evolving gene regulatory networks, our framework can detect the transition points between the developmental stages of *Drosophila Melanogaster*. Interestingly, these transition points agree with those obtained from the experimental results on the profiling of *Drosophila Melanogaster*. Therefore, from different perspectives than the

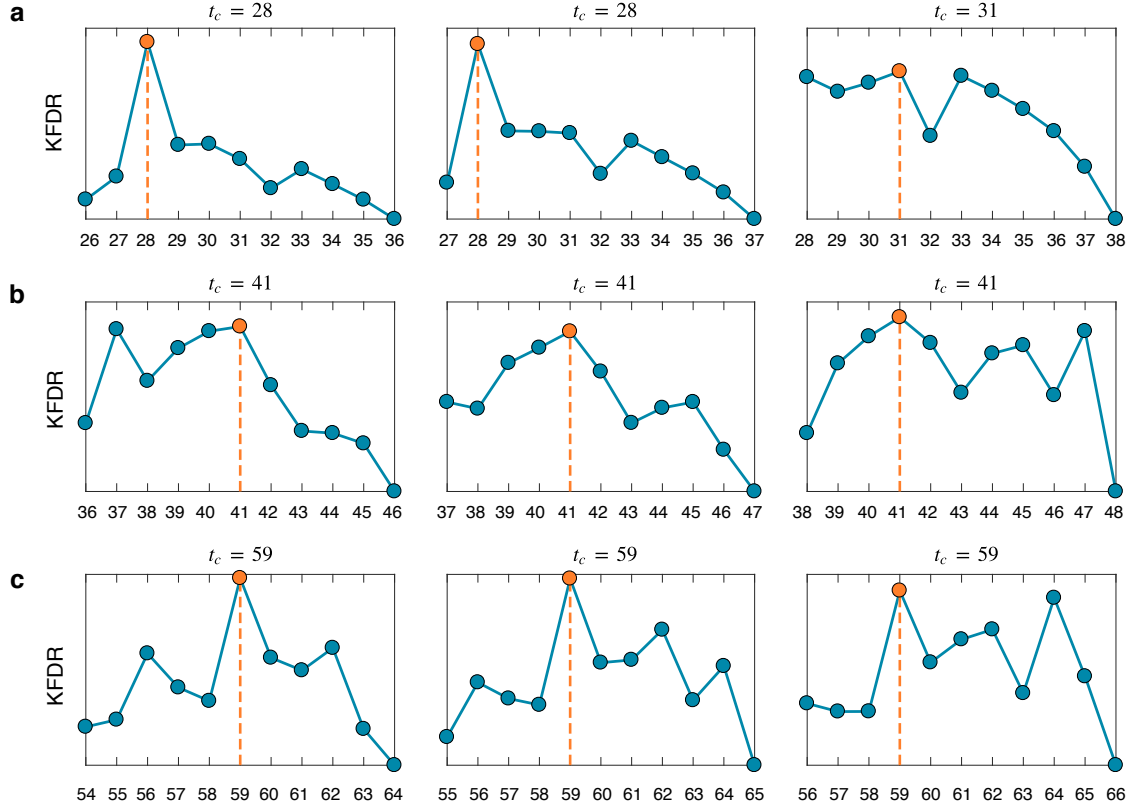


**Figure 5 | Kernel Fisher discriminant ratio (KFDR) calculated from three-dimensional persistence diagrams of one-dimensional holes for the time-evolving *Drosophila Melanogaster* gene regulatory networks.** We detect the transition time points in the windows of 11 time points spanning from different developmental stages. In each window, the transition time point  $t_c$  is the time index of the maximum KFDR value marked with the orange point. **(a)** The windows from the embryonic stage to the larval stage with time points  $26 \rightarrow 36$  ( $t_c = 28$ ),  $27 \rightarrow 37$  ( $t_c = 28$ ) and  $28 \rightarrow 38$  ( $t_c = 31$ ). **(b)** The windows from the larval stage to the pupal stage with time points  $36 \rightarrow 46$  ( $t_c = 41$ ),  $37 \rightarrow 47$  ( $t_c = 41$ ) and  $38 \rightarrow 48$  ( $t_c = 41$ ). **(c)** The windows from the pupal stage to the adulthood stage with time points  $54 \rightarrow 64$  ( $t_c = 59$ ),  $55 \rightarrow 65$  ( $t_c = 59$ ) and  $56 \rightarrow 66$  ( $t_c = 59$ ).

previous approaches, our findings indicate that understanding the variation of topological scales and the non-dyadic interactions can provide important insights into the behaviour of complex systems.

In our experiments, the scale-variant topological features were constructed from zero-dimensional and one-dimensional holes. In principle, we can compute the features from higher-dimensional holes that represent non-dyadic interactions involving a larger number of nodes in each interaction. However, to investigate the features from high-dimensional holes, the Vietoris–Rips filtration used in our study can consist of a large number of simplices. More precisely, to consider  $l$ -dimensional holes, the Vietoris–Rips filtration has size  $O(N^{l+1})$  of the number of simplices. This observation shows the difficulty of using the features from  $l$ -dimensional holes ( $l \geq 2$ ) for networks with a large number of nodes  $N$ . However, as demonstrated in this paper, we found that it is sufficient in practical applications to use  $l$ -dimensional holes with  $l = 0, 1$ . Furthermore, one can replace the Vietoris–Rips filtration with the Witness filtration<sup>54</sup> or the approximation of the Vietoris–Rips filtration<sup>55</sup> for more efficient computations.

Our work is expected to become a unified analysis of complex networks. This work opens up new possibilities for designing effective algorithms in network science. Such possibilities include investigation of more complicated network structures. For instance, we can employ the proposed framework to study different aspects of multiplex networks or apply it to the structural reducibility of a multilayer network while preserving its dynamics and function.

## Methods

**Network models.** We describe network models used in our experiments.

GN is a particular case of the planted  $l$ -partition model. We use the network with 128 nodes partitioned into four communities of size 32 and the average degree of 16. In the GN model, we focus on the ratio  $r$  between the probability of inter-community links ( $p_{\text{out}}$ ) and intra-community links ( $p_{\text{in}}$ ). We vary  $r = p_{\text{out}}/p_{\text{in}} = 0.01, 0.02, \dots, 1.0$  and generate 10 random realizations of the network for each value of  $r$ .

LFR is a model that generates a network with a priority known communities, and both the node degrees and the community size follow the power-law distribution. We focus on the mixing rate  $\mu$  ( $0 \leq \mu \leq 1.0$ ), where each node shares a fraction  $1 - \mu$  of links with the nodes inside its community and a fraction of  $\mu$  with the nodes outside its community. For the standard LFR model, we set the number of nodes as 128, the average and the maximum degrees as 16 and 32 and the minimum and the maximum community sizes as 16 and 32, respectively. The power-law exponent coefficients for the degree distribution, the community size distribution and the weights distribution are  $t_1 = -2, t_2 = -1$  and  $t_3 = 1$ , respectively. We vary the mixing rate as  $\mu = 0.01, 0.2, \dots, 1.0$  and use the program provided by ref.<sup>37</sup> to generate 10 random realizations of a network for each value of  $\mu$ .

We generate networks from the WS rewiring model with 128 nodes and rewiring probability  $\beta = 0.00, 0.01, \dots, 1.0$ , with 10 random realizations for each value of  $\beta$ .

The ER model is a classical model that generates random networks. We set the number of nodes as 128, vary the pair-link probability  $p_{\text{link}} = 0.020, 0.021, \dots, 0.1$  and generate 10 random realizations of the networks for each value of  $p_{\text{link}}$ .

We generate networks from the LFR–H model with the hierarchical structure of communities. The number of nodes is 300, the minimum and the maximum sizes of the micro-community are 10 and 50, the minimum and the maximum sizes of the macro-community are 20 and 80 and the average and the maximum degrees are 20 and 25, respectively. The power-law exponent coefficients for the degree distribution, the community size distribution and the weights distribution are the same as for the standard LFR model. We keep the mixing rate for the micro-communities as  $\mu_{\text{micro}} = 0.16$ , and vary the mixing value for the macro-communities as  $\mu_{\text{macro}} = 0.01, 0.02, \dots, 0.2$  with 20 random realizations for each value of  $\mu_{\text{macro}}$ .

Finally, SP is a model that generates hierarchical networks with 640 nodes and three community structures nested in one another. There are 64 communities of 10 nodes at the small-scale level, 16 communities of 40 nodes at the medium-scale level and 4 communities of 160 nodes at the large-scale level. There are two parameters; the average degree  $\bar{k}$ , which represents the density of the network, and  $\rho$ , which quantifies the separations between the three scales. We keep  $\bar{k} = 16$ , vary the parameter  $\rho = 0.05, 0.10, \dots, 2.0$  and use the program provided by ref.<sup>18</sup> to generate 10 random realizations of the networks at each value of  $\rho$ .

**Kernel method for three-dimensional persistence diagrams.** Given a positive bandwidth  $\sigma$  and the positive rescaling coefficient  $\xi$  introduced to adjust the scale difference between the point-wise distance and time, we define the kernel  $k_{\sigma, \xi}$  between two three-dimensional persistence diagrams,  $E$  and  $F$ , as

$$k_{\sigma, \xi}(E, F) = \frac{1}{\sigma\sqrt{2\pi}} \sum_{\mathbf{p} \in E, \mathbf{q} \in F} \left( e^{-\frac{d_{\xi}^2(\mathbf{p}, \mathbf{q})}{2\sigma^2}} - e^{-\frac{d_{\xi}^2(\mathbf{p}, \bar{\mathbf{q}})}{2\sigma^2}} \right), \quad (5)$$

where  $d_{\xi}^2(\mathbf{p}, \mathbf{q}) = |b_1 - b_2|^2 + |d_1 - d_2|^2 + \xi^2|\tau_1 - \tau_2|^2$ ,  $d_{\xi}^2(\mathbf{p}, \bar{\mathbf{q}}) = |b_1 - d_2|^2 + |d_1 - b_2|^2 + \xi^2|\tau_1 - \tau_2|^2$ , with  $\mathbf{p} = (b_1, d_1, \tau_1)$  and  $\mathbf{q} = (b_2, d_2, \tau_2)$ ,  $\bar{\mathbf{q}} = (d_2, b_2, \tau_2)$ . The normalized version of the kernel is defined by the normalization  $k_{\sigma, \xi}(E, F) \leftarrow k_{\sigma, \xi}(E, F) / \sqrt{k_{\sigma, \xi}(E, E)k_{\sigma, \xi}(F, F)}$ .

We set the rescale coefficient to  $\xi = \sigma$  and present here a heuristic method to select the bandwidth  $\sigma$ . Given the kernel values calculated from the three-dimensional persistence diagrams  $Dg_1^{(3)}, Dg_2^{(3)}, \dots, Dg_M^{(3)}$ , we denote  $\sigma_s^2 = \text{median}\{(b_i - b_j)^2 + (d_i - d_j)^2 \mid (b_i, d_i, \tau_i), (b_j, d_j, \tau_j) \in Dg_s^{(3)}\}$  with  $s = 1, 2, \dots, M$ . We set  $\sigma$  as  $\sigma^2 = \frac{1}{2} \text{median}\{\sigma_s^2 \mid s = 1, \dots, M\}$  such that  $2\sigma^2$  takes values close to many  $(b_i - b_j)^2 + (d_i - d_j)^2$  values.

**Common statistical measures for a network.** For each network, we calculate the following 16 common measures: the density (the ratio of the existing to the possible edges), the transitivity<sup>13</sup> (the proportion of triangles), the diameter (the maximum eccentricity), the radius (the minimum eccentricity), the degree assortativity coefficient<sup>56</sup>, the global efficiency<sup>57</sup>, the number of connected parts, the average number of triangles that include a node as a vertex, the average local efficiency<sup>57</sup>, the average edge betweenness centrality<sup>58</sup>, the average node betweenness centrality<sup>59</sup>, the average node closeness centrality<sup>59</sup>, the average eccentricity, the average shortest paths and the average degree centrality<sup>59</sup>. We normalize the measures in the range of  $[0, 1]$  using the min-max normalization (i.e.  $f = (f - f_{\min}) / (f_{\max} - f_{\min})$ , where  $f_{\min}, f_{\max}$  are the minimum and the maximum values of a measure in the data).

**Real-world network data.** For the classification task, we test on ten real-world network datasets of bioinformatics and social networks<sup>50</sup>. Supplementary Table 1 shows the aggregate statistics for these datasets.

The first dataset is MUTAG<sup>60</sup>; it consists of 188 networks of chemical compounds divided into two classes according to their mutagenic effect on a bacterium, i.e. mutagenic aromatic and heteroaromatic nitro compounds.

BZR, COX2, DHFR<sup>61</sup> datasets consist of 405 ligands for the benzodiazepine receptor (BZR), 467 cyclooxygenase-2 inhibitors (COX2) and 756 inhibitors of the dihydrofolate reductase (DHFR) come with 3D coordinates. In each of these datasets, the chemical compounds are divided into active and inactive compounds that we need to classify.

FRANKENSTEIN<sup>62</sup> is a modified version of BURST<sup>63</sup> dataset made of 4337 molecules with 2401 mutagens and 1936 nonmutagens to classify. Each molecule is represented as a small network whose vertices are labelled by the chemical atom symbol and edges by the bond type.

PROTEINS<sup>64</sup> is a dataset of 1113 proteins represented as networks, where the nodes are secondary structure elements and the edges represent the neighbourhood within the 3-D structure or along the amino acid chain. We classify the proteins into enzymes and non-enzymes.

NCII and NCI109<sup>65</sup> are datasets of chemical compounds with 4110 and 4127 compounds, respectively. We classify the compounds with the ability to suppress or inhibit the growth of a panel of human tumour cell lines.

IMDB-BINARY<sup>66</sup> is a dataset of 1000 movie collaboration ego-networks for each actor (actress) in Action and Romance genres from IMDB.com. For each network, two nodes representing actors or actresses are connected if they appear in the same movie. The task is to identify whether a given ego-network of an actor (actress) belongs to the Action or Comedy genre.

IMDB-MULTI<sup>66</sup> is the multi-class version of IMDB-BINARY and contains 1500 ego-networks belonging to Comedy, Romance and Sci-Fi genres.

**Code availability.** The C++ code for calculating the persistent diagrams (the core implementation referenced from Ripser library<sup>67</sup>) and the kernel, the Python code for mapping network nodes into a point cloud, the R code for calculating other graph kernel methods and the MATLAB code for generating network benchmarks are publicly available from the GitHub repository <https://github.com/OminiaVincit/scale-variant-topo>.

**Data availability.** The data that support the findings of this study are available from the corresponding author upon a reasonable request. However, the benchmark networks can be generated by using the source code in the ‘‘Code availability’’ section. For the real network data that have been obtained from publicly available sources, the corresponding URLs or references are provided in the ‘‘Real-world network data’’ section.

## References

1. Taylor, D. *et al.* Topological data analysis of contagion maps for examining spreading processes on networks. *Nat. Commun.* **6**, 7723 (2015).
2. Zañudo, J. G. T., Yang, G. & Albert, R. Structure-based control of complex networks with nonlinear dynamics. *Proc. Natl Acad. Sci. USA* **114**, 7234–7239 (2017).
3. Santolini, M. & Barabási, A.-L. Predicting perturbation patterns from the topology of biological networks. *Proc. Natl Acad. Sci. USA* **115**, E6375–E6383 (2018).
4. Sun, K., Gonçalves, J. P., Larminie, C. & Pržulj, N. Predicting disease associations via biological network analysis. *BMC Bioinformatics* **15**, 304 (2014).

5. Calderone, A. *et al.* Comparing alzheimer's and parkinson's diseases networks using graph communities structure. *BMC Syst. Biol.* **10**, 25 (2016).
6. Schieber, T. A. *et al.* Quantification of network structural dissimilarities. *Nat. Commun.* **8**, 13928 (2017).
7. Carpi, L., Saco, P., Rosso, O. & Ravetti, M. Structural evolution of the tropical pacific climate network. *Eur. Phys. J. B* **85**, 389 (2012).
8. Barnett, I. & Onnela, J.-P. Change point detection in correlation networks. *Sci. Rep.* **6**, 18893 (2016).
9. Bao, W. & Michailidis, G. Core community structure recovery and phase transition detection in temporally evolving networks. *Sci. Rep.* **8**, 12938 (2018).
10. Ahn, Y.-Y., Bagrow, J. P. & Lehmann, S. Link communities reveal multiscale complexity in networks. *Nature* **466**, 761 (2010).
11. Betzel, R. F. & Bassett, D. S. Multi-scale brain networks. *Neuroimage* **160**, 73–83 (2017).
12. Boulos, R. E., Tremblay, N., Arneodo, A., Borgnat, P. & Audit, B. Multi-scale structural community organisation of the human genome. *BMC Bioinformatics* **18**, 209 (2017).
13. Costa, L. d. F., Rodrigues, F. A., Traverso, G. & Villas Boas, P. R. Characterization of complex networks: A survey of measurements. *Adv. Phys.* **56**, 167–242 (2007).
14. Newman, M. E. J. *Networks: An Introduction* (Oxford Univ. Press, 2010).
15. Arenas, A., Díaz-Guilera, A. & Pérez-Vicente, C. J. Synchronization reveals topological scales in complex networks. *Phys. Rev. Lett.* **96**, 114102 (2006).
16. Sales-Pardo, M., Guimera, R., Moreira, A. A. & Amaral, L. A. N. Extracting the hierarchical organization of complex systems. *Proc. Natl Acad. Sci. USA* **104**, 15224–15229 (2007).
17. Lancichinetti, A., Fortunato, S. & Kertész, J. Detecting the overlapping and hierarchical community structure in complex networks. *New J. Phys.* **11**, 033015 (2009).
18. Tremblay, N. & Borgnat, P. Graph wavelets for multiscale community mining. *IEEE Trans. Signal Process.* **62**, 5227–5239 (2014).
19. Marvel, S. A., Kleinberg, J., Kleinberg, R. D. & Strogatz, S. H. Continuous-time model of structural balance. *Proc. Natl Acad. Sci. USA* **108**, 1771–1776 (2011).
20. van der Schaft, A., Rao, S. & Jayawardhana, B. On the mathematical structure of balanced chemical reaction networks governed by mass action kinetics. *SIAM J. Appl. Math.* **73**, 953–973 (2013).
21. Reimann, M. W. *et al.* Cliques of neurons bound into cavities provide a missing link between structure and function. *Frontiers in Computational Neuroscience* **48** (2017).
22. de Menezes, M. A. & Barabási, A.-L. Fluctuations in network dynamics. *Phys. Rev. Lett.* **92**, 028701 (2004).
23. Wells, D. K., Kath, W. L. & Motter, A. E. Control of stochastic and induced switching in biophysical networks. *Phys. Rev. X* **5**, 031036 (2015).
24. Hindes, J. & Schwartz, I. B. Epidemic extinction and control in heterogeneous networks. *Phys. Rev. Lett.* **117**, 028302 (2016).
25. Barabási, A.-L. *et al.* *Network science* (Cambridge Univ. Press, 2016).
26. Edelsbrunner, H. & Harer, J. *Computational Topology. An Introduction.* (Amer. Math. Soc., 2010).
27. Edelsbrunner, H., Letscher, D. & Zomorodian, A. Topological persistence and simplification. *Discrete Comput. Geom.* **28**, 511–533 (2002).
28. Zomorodian, A. & Carlsson, G. Computing persistent homology. *Discrete Comput. Geom.* **33**, 249–274 (2005).
29. Carlsson, G. Topology and data. *Bull. Amer. Math. Soc.* **46**, 255–308 (2009).
30. Kaczynski, T., Mischaikow, K. & Mrozek, M. *Computational homology*, vol. 157 (Springer, 2006).
31. Mischaikow, K. & Nanda, V. Morse theory for filtrations and efficient computation of persistent homology. *Discrete Comput. Geom.* **50**, 330–353 (2013).

32. Tran, Q. H. & Hasegawa, Y. Topological time-series analysis with delay-variant embedding (2018). Preprint at [arXiv:1803.00208](https://arxiv.org/abs/1803.00208).
33. Harchaoui, Z., Moulines, E. & Bach, F. R. Kernel change-point analysis. In *Adv. Neural Inf. Process. Syst.*, 609–616 (2009).
34. Chazal, F., de Silva, V. & Oudot, S. Persistence stability for geometric complexes. *Geometriae Dedicata* **173**, 193–214 (2014).
35. Golub, G. H. & Van Loan, C. F. *Matrix computations*, vol. 3 (JHU Press, 2012).
36. Newman, M. E. J. & Girvan, M. Finding and evaluating community structure in networks. *Phys. Rev. E* **69**, 026113 (2004).
37. Lancichinetti, A., Fortunato, S. & Radicchi, F. Benchmark graphs for testing community detection algorithms. *Phys. Rev. E* **78**, 046110 (2008).
38. Lancichinetti, A. & Fortunato, S. Benchmarks for testing community detection algorithms on directed and weighted graphs with overlapping communities. *Phys. Rev. E* **80**, 016118 (2009).
39. Erdős, P. & Rényi, A. On random graphs I. *Publ. Math.* **6**, 290–297 (1959).
40. Watts, D. J. & Strogatz, S. H. Collective dynamics of ‘small-world’ networks. *Nature* **393**, 440–442 (1998).
41. Newman, M. E. J., Strogatz, S. H. & Watts, D. J. Random graphs with arbitrary degree distributions and their applications. *Phys. Rev. E* **64**, 026118 (2001).
42. Bishop, C. M. *Pattern Recognition and Machine Learning (Information Science and Statistics)* (Springer, 2006).
43. Kashima, H., Tsuda, K. & Inokuchi, A. Marginalized kernels between labeled graphs. In *Proceedings of the 20th International Conference on Machine Learning*, 321–328 (2003).
44. Gärtner, T., Flach, P. & Wrobel, S. On graph kernels: Hardness results and efficient alternatives. In *Proceedings of the 16th Annual Conference on Computational Learning Theory*, 129–143 (2003).
45. Borgwardt, K. M. & Kriegel, H.-P. Shortest-path kernels on graphs. In *Proceedings of the 5th IEEE International Conference on Data Mining*, 74–81 (2005).
46. Borgwardt, K. M., Petri, T., Vishwanathan, S. & Kriegel, H.-P. An efficient sampling scheme for comparison of large graphs. *MLG* (2007).
47. Shervashidze, N., Schweitzer, P., Leeuwen, E. J. v., Mehlhorn, K. & Borgwardt, K. M. Weisfeiler–Lehman graph kernels. *JMLR* **12**, 2539–2561 (2011).
48. Sugiyama, M., Ghisu, M. E., Llinares-López, F. & Borgwardt, K. graphkernels: R and python packages for graph comparison. *Bioinformatics* **34**, 530–532 (2017).
49. De Domenico, M. Diffusion geometry unravels the emergence of functional clusters in collective phenomena. *Phys. Rev. Lett.* **118**, 168301 (2017).
50. Kersting, K., Kriege, N. M., Morris, C., Mutzel, P. & Neumann, M. Benchmark data sets for graph kernels (2016). <http://graphkernels.cs.tu-dortmund.de>.
51. Arbeitman, M. N. *et al.* Gene expression during the life cycle of *Drosophila melanogaster*. *Science* **297**, 2270–2275 (2002).
52. Zhang, J. & Cao, J. Finding common modules in a time-varying network with application to the *Drosophila melanogaster* gene regulation network. *J. Am. Stat. Assoc.* **112**, 994–1008 (2017).
53. Song, L., Kolar, M. & Xing, E. P. Keller: estimating time-varying interactions between genes. *Bioinformatics* **25**, i128–i136 (2009).
54. De Silva, V. & Carlsson, G. E. Topological estimation using witness complexes. *SPBG* **4**, 157–166 (2004).
55. Sheehy, D. R. Linear-size approximations to the Vietoris–Rips filtration. *Discrete Comput. Geom.* **49**, 778–796 (2013).
56. Newman, M. E. J. Assortative mixing in networks. *Phys. Rev. Lett.* **89**, 208701 (2002).
57. Latora, V. & Marchiori, M. Efficient behavior of small-world networks. *Phys. Rev. Lett.* **87**, 198701 (2001).

58. Brandes, U. On variants of shortest-path betweenness centrality and their generic computation. *Soc. Networks* **30**, 136–145 (2008).
59. Freeman, L. C. Centrality in social networks conceptual clarification. *Soc. Networks* **1**, 215–239 (1978).
60. Debnath, A. K., Lopez de Compadre, R. L., Debnath, G., Shusterman, A. J. & Hansch, C. Structure-activity relationship of mutagenic aromatic and heteroaromatic nitro compounds. Correlation with molecular orbital energies and hydrophobicity. *J. Med. Chem.* **34**, 786–797 (1991).
61. Sutherland, J. J., O’Brien, L. A. & Weaver, D. F. Spline-fitting with a genetic algorithm: A method for developing classification structure-activity relationships. *J. Chem. Inf. Comput. Sci.* **43**, 1906–1915 (2003).
62. Orsini, F., Frasconi, P. & De Raedt, L. Graph invariant kernels. In *Proceedings of the 24th International Joint Conference on Artificial Intelligence*, 3756–3762 (2015).
63. Kazius, J., McGuire, R. & Bursi, R. Derivation and validation of toxicophores for mutagenicity prediction. *J. Med. Chem.* **48**, 312–320 (2005).
64. Borgwardt, K. M. *et al.* Protein function prediction via graph kernels. *Bioinformatics* **21**, i47–i56 (2005).
65. Wale, N., Watson, I. A. & Karypis, G. Comparison of descriptor spaces for chemical compound retrieval and classification. *Knowledge and Information Systems* **14**, 347–375 (2008).
66. Yanardag, P. & Vishwanathan, S. Deep graph kernels. In *Proceedings of the 21th ACM SIGKDD International Conference on Knowledge Discovery and Data Mining*, 1365–1374 (2015).
67. Bauer, U. Ripser: a lean C++ code for the computation of Vietoris–Rips persistence barcodes (2017). <https://github.com/Ripser/ripser>.

# Supplemental Material for “Scale-variant Topological Information for Characterizing Complex Networks”

Quoc Hoan Tran, Van Tuan Vo and Yoshihiko Hasegawa

This supplementary material describes in detail the calculations introduced in the main text and additional figures. Equations in this section are prefixed with S (e.g. Eq. (S1)). Numbers without the prefix (e.g. Eq. (1)) refer to items in the main text.

## Supplementary Notes.

### Supplementary Note 1: Construction of Vietoris–Rips filtration of a network.

In the following sections, we define and describe in Supplementary Fig. 1 the process of extracting topological features of a complex network at each specific timescale  $\tau$ .

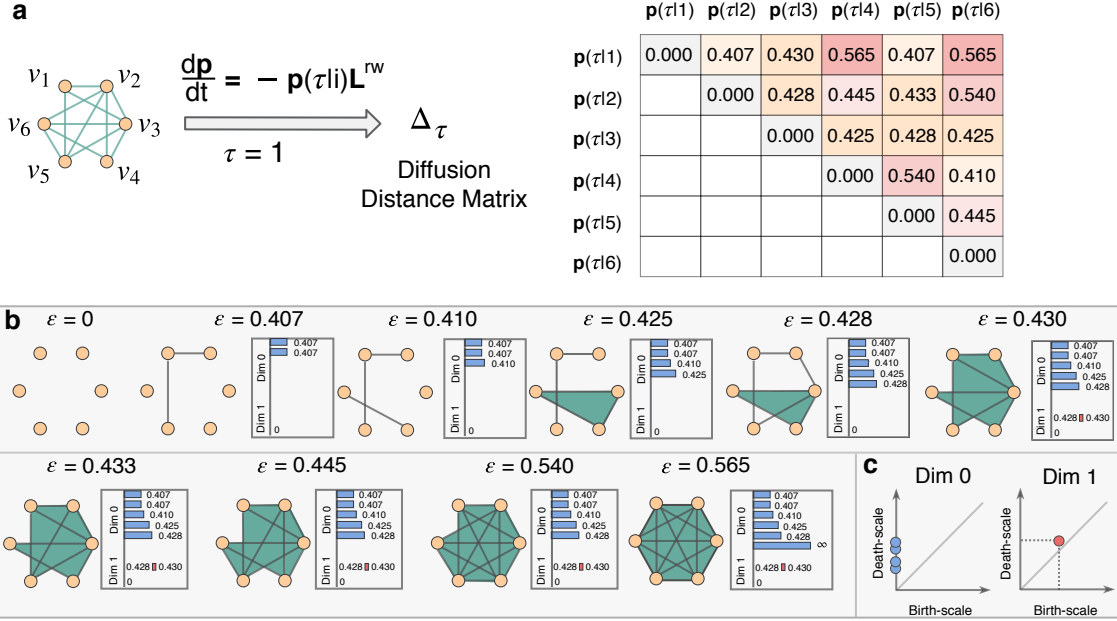
We consider an undirected weighted network  $\mathcal{G}$  with  $N$  nodes  $v_1, \dots, v_N$ . We denote  $\mathbf{L}_{\mathcal{G}}^{\text{rw}}$  as the random walk Laplacian of network  $\mathcal{G}$ . At a specific  $\tau$ , we map the nodes of network  $\mathcal{G}$  to a point cloud of  $N$  points  $\mathbf{p}_{\mathcal{G}}(\tau|1), \dots, \mathbf{p}_{\mathcal{G}}(\tau|N)$ . Here,  $\mathbf{p}_{\mathcal{G}}(\tau|i)$  is given according to the solution of the Kolmogorov forward equation:

$$\frac{d\mathbf{p}_{\mathcal{G}}(\tau|i)}{dt} = -\mathbf{p}_{\mathcal{G}}(\tau|i)\mathbf{L}_{\mathcal{G}}^{\text{rw}}. \quad (\text{S1})$$

The solution for Eq. (S1) is  $\mathbf{p}_{\mathcal{G}}(\tau|i) = \mathbf{u}_i \exp(-\tau\mathbf{L}_{\mathcal{G}}^{\text{rw}})$ , where  $\mathbf{u}_i = [0, \dots, 0, 1, 0, \dots, 0]$  with its  $i$ -th element being equal to 1; others are equal to 0.

At each  $\tau$ , we calculate the diffusion distance matrix  $\Delta_{\tau}$  of size  $N \times N$ , whose element  $\Delta_{ij}$  is the Euclidean distance between points  $\mathbf{p}_{\mathcal{G}}(\tau|i)$  and  $\mathbf{p}_{\mathcal{G}}(\tau|j)$  (Supplementary Fig. 1a). If  $\varepsilon = 0$ , the nodes of the network can be considered discrete points. As we increase  $\varepsilon$ , new pairwise connections and simplices may appear when  $\varepsilon$  meets each value of  $\Delta_{ij}$ . We obtain a filtration as a sequence of embedded simplicial complexes. Hole patterns such as connected components or loops can appear or disappear over this filtration. For instance, in Supplementary Fig. 1b, at  $\varepsilon = 0$ , we have six separated nodes considered as six separated connected components, but at  $\varepsilon = 0.407$ , three nodes are connected with each other; thus, two connected components disappear at this scale. We can describe these patterns as two blue bars started at scale 0 and ended at scale 0.407. The same explanation with the red bar started at scale 0.428 and ended at scale 0.430, which represents the emergence of loop pattern ( $v_1 \rightarrow v_2 \rightarrow v_3 \rightarrow v_5 \rightarrow v_1$ ) at  $\varepsilon = 0.428$  and the disappearance at  $\varepsilon = 0.430$ . Supplementary Figure 1c illustrates the corresponding persistence diagrams for zero-dimensional holes and one-dimensional holes, where the birth-scale and the death-scale are represented for the values of  $\varepsilon$  at the emergence and the disappearance of the holes.





**Supplementary Figure 1 | Construction of Vietoris–Rips filtration of a complex network at a specific timescale  $\tau$ .** We map nodes  $v_1, \dots, v_N$  of the network to a point cloud of  $N$  points  $p(\tau|1), \dots, p(\tau|N)$  through a diffusion dynamics described by the random walk Laplacian  $L^{rw}$ . **(a)** Diffusion distance matrix  $\Delta_\tau$  of size  $N \times N$ , whose element  $\Delta_{ij}$  is the Euclidean distance between points  $p(\tau|i)$  and  $p(\tau|j)$ . **(b)** A complex is built over a set of points if the pairwise distances between them are less than or equal to a distance-scale parameter  $\varepsilon$ . If  $\varepsilon = 0$ , we have the discrete points. As  $\varepsilon$  takes the increasing sequence values of diffusion distance  $\Delta_{ij}$ , the hole patterns such as connected components (zero-dimensional hole) or loops (one-dimensional hole) can appear or disappear over this filtration. The lifetime of these hole patterns are described as blue bars (for zero-dimensional holes) and red bars (for one-dimensional holes). These bars begin at the values of  $\varepsilon$  when the holes appear, then end at values when the holes disappear. **(c)** The corresponding persistence diagrams for zero-dimensional and one-dimensional holes. The birth-scale and the death-scale are represented for the values of  $\varepsilon$  at the emergence and the disappearance of the holes.

## Supplementary Note 2: Kernel Fisher discriminant ratio.

The kernel method maps persistence diagrams in an abstract space, namely, a reproducing Hilbert space  $\mathcal{H}$  associated with a reproducing kernel  $k(\cdot, \cdot)$  and a feature map  $\Phi(DgX) = k(DgX, \cdot)$ . The inner product between two operators  $\Phi(DgX)$  and  $\Phi(DgY)$  is defined as  $\langle \Phi(DgX), \Phi(DgY) \rangle_{\mathcal{H}} = k(DgX, DgY)$ . Here,  $DgX$  and  $DgY$  are two three-dimensional persistence diagrams. We consider a window as a collection of diagrams  $\mathcal{D} = \{Dg_1, \dots, Dg_M\}$  and a given index  $s > 1$ . The corresponding empirical mean elements and covariance operators associated with the data in  $\mathcal{D}$  having index before and from  $s$  are defined as

$$\hat{\mu}_1 = \frac{1}{s-1} \sum_{i=1}^{s-1} k(Dg_i, \cdot), \quad (\text{S2})$$

$$\hat{\Sigma}_1 = \frac{1}{s-1} \sum_{i=1}^{s-1} \{k(Dg_i, \cdot) - \hat{\mu}_1\} \otimes \{k(Dg_i, \cdot) - \hat{\mu}_1\}, \quad (\text{S3})$$

$$\hat{\mu}_2 = \frac{1}{M-s+1} \sum_{i=s}^M k(Dg_i, \cdot), \quad (\text{S4})$$

$$\hat{\Sigma}_2 = \frac{1}{M-s+1} \sum_{i=s}^M \{k(Dg_i, \cdot) - \hat{\mu}_2\} \otimes \{k(Dg_i, \cdot) - \hat{\mu}_2\}. \quad (\text{S5})$$

Here,  $f \otimes g$  for two operators  $f, g \in \mathcal{H}$  is defined for all operators  $h \in \mathcal{H}$  as  $(f \otimes g)h = \langle g, h \rangle_{\mathcal{H}} f$ .

The kernel Fisher discriminant ratio  $\text{KFDR}_{M,s}(\mathcal{D})$ <sup>3</sup> is defined as

$$\text{KFDR}_{M,s}(\mathcal{D}) = \frac{(s-1)(M-s+1)}{M} \left\langle \hat{\mu}_2 - \hat{\mu}_1, (\hat{\Sigma} + \gamma \mathbf{I})^{-1} (\hat{\mu}_2 - \hat{\mu}_1) \right\rangle_{\mathcal{H}}, \quad (\text{S6})$$

where  $\gamma$  is a regularization parameter and  $\hat{\Sigma} = \frac{s-1}{M} \hat{\Sigma}_1 + \frac{M-s+1}{M} \hat{\Sigma}_2$ .

We set  $\gamma = 10^{-1}, 10^{-1}, 10^{-5}$  in the experiments of the Girvan–Newman (GN) network, Lancichinetti–Fortunato–Radicchi (LFR) network and *Drosophila Melanogaster* network, respectively.

## Supplementary Note 3: Stability of scale-variant topological features.

To prove the stability property of the topological features undergoing network perturbation, we introduce the concept of the bottleneck distance between two two-dimensional diagrams first. Let  $X$  and  $Y$  be finite sets of points embedded in the Euclidean space  $\mathbb{R}^n$ . Denote their *two*-dimensional persistent diagrams for  $l$ -dimensional holes as  $DgX$  and  $DgY$ , respectively. We consider all matchings,  $\gamma$ , such that a point on one diagram is matched to a point on the other diagram or to its projection on the line  $b = d$  in two-dimensional space. The bottleneck distance  $d_B^{(2)}$  between  $DgX$  and  $DgY$  is defined as the infimum of the longest matched infinity-norm distance over all matchings,  $\gamma$ :

$$d_B^{(2)}(DgX, DgY) = \inf_{\gamma} \max_{(\mathbf{p}, \mathbf{q}) \in \gamma} \|\mathbf{p} - \mathbf{q}\|_{\infty}. \quad (\text{S7})$$

The bottleneck distance between the two-dimensional persistence diagrams satisfies the following inequality<sup>1</sup>:

$$d_B^{(2)}(DgX, DgY) \leq 2d_H(X, Y), \quad (\text{S8})$$

where  $d_H(X, Y)$  is the Hausdorff distance given as

$$d_H(X, Y) = \max \left\{ \max_{\mathbf{x} \in X} \min_{\mathbf{y} \in Y} d(\mathbf{x}, \mathbf{y}), \max_{\mathbf{y} \in Y} \min_{\mathbf{x} \in X} d(\mathbf{x}, \mathbf{y}) \right\}. \quad (\text{S9})$$

Here,  $d(\mathbf{x}, \mathbf{y})$  is the Euclidean distance between two points  $\mathbf{x}, \mathbf{y}$  in  $\mathbb{R}^n$ .

Given two three-dimensional persistence diagrams as  $E$  and  $F$ , consider all matchings  $\psi$  such that a point on one diagram is matched to a point on the other diagram or to its projection on the plane  $b = d$ . For each pair  $(\mathbf{p}, \mathbf{q}) \in \psi$  for which  $\mathbf{p} = (b_1, d_1, \tau_1)$  and  $\mathbf{q} = (b_2, d_2, \tau_2)$ , we define the *relative infinity-norm distance* between  $\mathbf{p}$  and  $\mathbf{q}$  as  $d_{\xi}^{(\infty)}(\mathbf{p}, \mathbf{q}) = \max(|b_1 - b_2|, |d_1 - d_2|, \xi|\tau_1 - \tau_2|)$ , where  $\xi$  is a positive rescaling coefficient introduced to adjust the scale difference between the point-wise distance and time. The bottleneck distance,  $d_{B,\xi}^{(3)}(E, F)$ , is defined as the infimum of the longest matched relative infinity-norm distance over all matchings,  $\psi$ :

$$d_{B,\xi}^{(3)}(E, F) = \inf_{\psi} \max_{(\mathbf{p}, \mathbf{q}) \in \psi} d_{\xi}^{(\infty)}(\mathbf{p}, \mathbf{q}). \quad (\text{S10})$$

For each  $\tau \in \mathcal{T}$  and two networks  $\mathcal{G}, \mathcal{H}$  with the same number  $N$  of nodes, we first prove the following inequality:

$$d_B^{(2)}(Dg_{l,\tau}^{(2)}(\mathcal{G}), Dg_{l,\tau}^{(2)}(\mathcal{H})) \leq 2\tau \|\mathbf{L}_{\mathcal{G}}^{\text{rw}} - \mathbf{L}_{\mathcal{H}}^{\text{rw}}\|_2. \quad (\text{S11})$$

Here, two two-dimensional persistence diagrams  $Dg_{l,\tau}^{(2)}(\mathcal{G})$  and  $Dg_{l,\tau}^{(2)}(\mathcal{H})$  are calculated for  $l$ -dimensional holes from two point clouds  $\mathbf{P}_{\mathcal{G},\tau} = \{\mathbf{p}_{\mathcal{G}}(\tau|1), \dots, \mathbf{p}_{\mathcal{G}}(\tau|N)\}$  and  $\mathbf{P}_{\mathcal{H},\tau} = \{\mathbf{p}_{\mathcal{H}}(\tau|1), \dots, \mathbf{p}_{\mathcal{H}}(\tau|N)\}$ , respectively.

By applying Eq. (S8) with  $\mathbf{P}_{\mathcal{G},\tau}$  and  $\mathbf{P}_{\mathcal{H},\tau}$ , we have

$$d_B^{(2)}(Dg_{l,\tau}^{(2)}(\mathcal{G}), Dg_{l,\tau}^{(2)}(\mathcal{H})) \leq 2d_H(\mathbf{P}_{\mathcal{G},\tau}, \mathbf{P}_{\mathcal{H},\tau}), \quad (\text{S12})$$

From the definition of the Hausdorff distance, we have

$$d_H(\mathbf{P}_{\mathcal{G},\tau}, \mathbf{P}_{\mathcal{H},\tau}) = \max \left\{ \max_i \min_j d(\mathbf{p}_{\mathcal{G}}(\tau|i), \mathbf{p}_{\mathcal{H}}(\tau|j)), \max_j \min_i d(\mathbf{p}_{\mathcal{G}}(\tau|i), \mathbf{p}_{\mathcal{H}}(\tau|j)) \right\} \quad (\text{S13})$$

$$\leq \max \left\{ \max_i d(\mathbf{p}_{\mathcal{G}}(\tau|i), \mathbf{p}_{\mathcal{H}}(\tau|i)), \max_j d(\mathbf{p}_{\mathcal{G}}(\tau|j), \mathbf{p}_{\mathcal{H}}(\tau|j)) \right\} \quad (\text{S14})$$

$$= \max_i d(\mathbf{p}_{\mathcal{G}}(\tau|i), \mathbf{p}_{\mathcal{H}}(\tau|i)). \quad (\text{S15})$$

Since  $\mathbf{p}_{\mathcal{G}}(\tau|i) = \mathbf{u}_i \exp(-\tau \mathbf{L}_{\mathcal{G}}^{\text{rw}})$  and  $\mathbf{p}_{\mathcal{H}}(\tau|i) = \mathbf{u}_i \exp(-\tau \mathbf{L}_{\mathcal{H}}^{\text{rw}})$ , we have

$$d(\mathbf{p}_{\mathcal{G}}(\tau|i), \mathbf{p}_{\mathcal{H}}(\tau|i)) = \|\mathbf{u}_i (e^{-\tau \mathbf{L}_{\mathcal{G}}^{\text{rw}}} - e^{-\tau \mathbf{L}_{\mathcal{H}}^{\text{rw}}})\|_2 \quad (\text{S16})$$

$$\leq \|\mathbf{u}_i\|_2 \|e^{-\tau \mathbf{L}_{\mathcal{G}}^{\text{rw}}} - e^{-\tau \mathbf{L}_{\mathcal{H}}^{\text{rw}}}\|_2 = \|e^{-\tau \mathbf{L}_{\mathcal{G}}^{\text{rw}}} - e^{-\tau \mathbf{L}_{\mathcal{H}}^{\text{rw}}}\|_2. \quad (\text{S17})$$

We write the difference of the matrix exponential in terms of an integral<sup>2</sup>,

$$\|e^{-\tau \mathbf{L}_{\mathcal{G}}^{\text{rw}}} - e^{-\tau \mathbf{L}_{\mathcal{H}}^{\text{rw}}}\|_2 = \left\| \int_0^\tau e^{-\mathbf{L}_{\mathcal{G}}^{\text{rw}}(\tau-t)} \mathbf{E} e^{-\mathbf{L}_{\mathcal{H}}^{\text{rw}}t} dt \right\|_2 \quad (\text{S18})$$

$$\leq \int_0^\tau \|e^{-\mathbf{L}_{\mathcal{G}}^{\text{rw}}(\tau-t)} \mathbf{E} e^{-\mathbf{L}_{\mathcal{H}}^{\text{rw}}t}\|_2 dt \leq \|\mathbf{E}\|_2 \int_0^\tau \|e^{-\mathbf{L}_{\mathcal{G}}^{\text{rw}}(\tau-t)}\|_2 \|e^{-\mathbf{L}_{\mathcal{H}}^{\text{rw}}t}\|_2 dt, \quad (\text{S19})$$

where  $\mathbf{E} = \mathbf{L}_{\mathcal{G}}^{\text{rw}} - \mathbf{L}_{\mathcal{H}}^{\text{rw}}$ . We know that  $-\mathbf{L}_{\mathcal{G}}^{\text{rw}}$  is a negative semi-definite matrix with the largest eigenvalue equal to 0. It implies that the largest eigenvalue of  $e^{-\mathbf{L}_{\mathcal{G}}^{\text{rw}}(\tau-t)}$  is equal to 1, and hence  $\|e^{-\mathbf{L}_{\mathcal{G}}^{\text{rw}}(\tau-t)}\|_2 = 1$ . We obtain the same result with  $-\mathbf{L}_{\mathcal{H}}^{\text{rw}}$ , i.e.  $\|e^{-\mathbf{L}_{\mathcal{H}}^{\text{rw}}t}\|_2 = 1$ . Then, from Eq. (S17) and Eq. (S19), we have

$$d(\mathbf{p}_{\mathcal{G}}(\tau|i), \mathbf{p}_{\mathcal{H}}(\tau|i)) \leq \|\mathbf{E}\|_2 \int_0^\tau 1 dt = \tau \|\mathbf{E}\|_2 = \tau \|\mathbf{L}_{\mathcal{G}}^{\text{rw}} - \mathbf{L}_{\mathcal{H}}^{\text{rw}}\|_2. \quad (\text{S20})$$

From Eq. (S12), Eq. (S15) and Eq. (S20), we have the result in Eq. (S11).

Let  $\Gamma_\tau$  be the set of matchings defined in Eq. (S7) between two two-dimensional persistence diagrams  $Dg_{l,\tau}^{(2)}(\mathcal{G})$  and  $Dg_{l,\tau}^{(2)}(\mathcal{H})$ . For each collection  $\Lambda = \{\gamma_1, \gamma_2, \dots, \gamma_K \mid \gamma_i \in \Gamma_{\tau_i}, i = 1, 2, \dots, K\}$ , we consider the matching  $\psi$  between two three-dimensional persistence diagrams  $Dg_l^{(3)}(\mathcal{G})$  and  $Dg_l^{(3)}(\mathcal{H})$  constructed in the following way. For each  $(\mathbf{p}, \mathbf{q}) \in \psi$ ,  $\mathbf{p} = (b_1, d_1, \tau)$ ,  $\mathbf{q} = (b_2, d_2, \tau)$  and  $(\mathbf{p}_\gamma, \mathbf{q}_\gamma) \in \gamma$ , where  $\mathbf{p}_\gamma = (b_1, d_1)$ ,  $\mathbf{q}_\gamma = (b_2, d_2)$  and  $\gamma \in \Lambda \cap \Gamma_\tau$ . Let  $\Gamma$  be a set of all matchings  $\psi$  constructed this way. From the definition of the bottleneck distance, we have the following inequality:

$$d_{B,\xi}^{(3)}(Dg_l^{(3)}(\mathcal{G}), Dg_l^{(3)}(\mathcal{H})) \leq \inf_{\psi \in \Gamma} \max_{(\mathbf{p}, \mathbf{q}) \in \psi} d_\xi^{(\infty)}(\mathbf{p}, \mathbf{q}). \quad (\text{S21})$$

For  $(\mathbf{p}, \mathbf{q}) \in \psi$ , we have

$$d_\xi^{(\infty)}(\mathbf{p}, \mathbf{q}) = \max\{|b_1 - b_2|, |d_1 - d_2|, \xi|\tau - \tau|\} \quad (\text{S22})$$

$$= \max\{|b_1 - b_2|, |d_1 - d_2|\} = \|\mathbf{p}_\gamma - \mathbf{q}_\gamma\|_\infty, \quad (\text{S23})$$

and Eq. (S21) becomes

$$d_{B,\xi}^{(3)}(Dg_l^{(3)}(\mathcal{G}), Dg_l^{(3)}(\mathcal{H})) \leq \max_{\tau \in \mathcal{T}} \inf_{\gamma \in \Gamma_\tau} \max_{(\mathbf{p}_\gamma, \mathbf{q}_\gamma) \in \gamma} \|\mathbf{p}_\gamma - \mathbf{q}_\gamma\|_\infty \quad (\text{S24})$$

$$= \max_{\tau \in \mathcal{T}} d_B^{(2)}(Dg_{l,\tau}^{(2)}(\mathcal{G}), Dg_{l,\tau}^{(2)}(\mathcal{H})). \quad (\text{S25})$$

From Eq. (S11) and Eq. (S25), we obtain Eq. (4) in the main text, which is the stability property of our scale-variant features.

## Supplementary Note 4: Graph kernel methods.

We describe the graph kernel methods used in the main text. These graph kernels are based on random walks (KStepRW, GeometricRW, ExponentialRW)<sup>4,5</sup>, paths (ShortestPath<sup>6</sup>), limited-sized subgraphs (Graphlet<sup>7</sup>) and subtree patterns (Weisfeiler–Lehman<sup>8</sup>). The implementations of these graph kernels can be found in ref.<sup>9</sup>.

**KStepRW kernel.** To measure the similarity between two graphs, the random walk graph kernel computes the number of equal-length walks in two graphs. Given two unlabeled graphs  $\mathcal{G}$  and  $\mathcal{G}'$  with their vertex and edge sets as  $(\mathcal{V}, \mathcal{E})$  and  $(\mathcal{V}', \mathcal{E}')$ , respectively, the direct product graph  $\mathcal{G}_\times = (\mathcal{V}_\times, \mathcal{E}_\times)$  of  $\mathcal{G}$  and  $\mathcal{G}'$  is a graph with the node set  $\mathcal{V}_\times = \{(v, v') \mid v \in \mathcal{V}, v' \in \mathcal{V}'\}$  and the edge set  $\mathcal{E}_\times = \{((v_a, v'_a), (v_b, v'_b)) \mid (v_a, v_b) \in \mathcal{E}, (v'_a, v'_b) \in \mathcal{E}'\}$ . The KStepRW kernel is the  $k$ -step random walk kernel  $\mathcal{K}_\times^k$  defined as

$$\mathcal{K}_\times^k(\mathcal{G}, \mathcal{G}') = \sum_{i,j=1}^{|\mathcal{V}_\times|} \sum_{m=0}^k [\lambda_m \mathbf{W}_\times^m]_{ij}, \quad (\text{S26})$$

where  $\mathbf{W}_\times$  is a weight matrix of  $\mathcal{G}_\times$  and  $\lambda_0, \dots, \lambda_k$  is a sequence of positive, real-valued weights. In our experiments, we set  $k = 2$  and  $\lambda_0 = \lambda_1 = \lambda_2 = 1.0$ .

**GeometricRW kernel.** This kernel is a specific case of the  $k$ -step random walk kernel, when  $k$  goes to infinity and the weights are the geometric series, i.e.  $\lambda_m = \lambda^m$  ( $\lambda = 0.05$  in our experiments). The GeometricRW kernel is defined as

$$\mathcal{K}_{\text{GR}}(\mathcal{G}, \mathcal{G}') = \sum_{i,j=1}^{|\mathcal{V}_\times|} \sum_{m=0}^{\infty} [\lambda^m \mathbf{W}_\times^m]_{ij} = \sum_{i,j=1}^{|\mathcal{V}_\times|} [(\mathbf{I} - \lambda \mathbf{W}_\times)^{-1}]_{ij}, \quad (\text{S27})$$

where  $\mathbf{I}$  is an identity matrix of size  $|\mathcal{V}_\times| \times |\mathcal{V}_\times|$ .

**ExponentialRW kernel.** This kernel is a specific case of the  $k$ -step random walk kernel, when  $k$  goes to infinity and the weights are the exponential series, i.e.  $\lambda_m = \frac{\beta^m}{m!}$  ( $\beta = 0.1$  in our experiments). ExponentialRW kernel is defined as

$$\mathcal{K}_{\text{ER}}(\mathcal{G}, \mathcal{G}') = \sum_{i,j=1}^{|\mathcal{V}_\times|} \sum_{m=0}^{\infty} \left[ \frac{(\beta \mathbf{W}_\times)^m}{m!} \right]_{ij} = \sum_{i,j=1}^{|\mathcal{V}_\times|} [e^{\beta \mathbf{W}_\times}]_{ij}. \quad (\text{S28})$$

**ShortestPath kernel.** This kernel compares all pairs of the shortest path lengths from  $\mathcal{G}$  and  $\mathcal{G}'$  defined as

$$\mathcal{K}_{\text{SP}}(\mathcal{G}, \mathcal{G}') = \sum_{v_i, v_j \in \mathcal{G}} \sum_{v'_k, v'_l \in \mathcal{G}'} \delta(d(v_i, v_j), d(v'_k, v'_l)), \quad (\text{S29})$$

where  $d(v_i, v_j)$  and  $d(v'_k, v'_l)$  are the lengths of the shortest path between nodes  $v_i$  and  $v_j$  in  $\mathcal{G}$ , and the shortest path between nodes  $v'_k$  and  $v'_l$  in  $\mathcal{G}'$ , respectively. Here, the  $\delta$ -function is defined as  $\delta(x, y) = 1$  if  $x = y$ , and 0 if  $x \neq y$ .

**Graphlet kernel.** A size- $k$  graphlet is an induced and non-isomorphic sub-graph of size  $k$ . Let  $\mathcal{S}_k = \{G_1, \dots, G_{N_k}\}$  be a set of size- $k$  graphlets, where  $N_k$  denotes the number of unique graphlets of size  $k$ . For an unlabeled graph  $\mathcal{G}$ , we define a vector  $\mathbf{f}_\mathcal{G}$  of length  $N_k$  such that the  $i^{\text{th}}$  component of  $\mathbf{f}_\mathcal{G}$  denotes the frequency of graphlet  $G_i$  appearing as a subgraph of  $\mathcal{G}$ . Given two unlabeled graphs  $\mathcal{G}$  and  $\mathcal{G}'$ , the graphlet kernel is defined as

$$\mathcal{K}_{\text{GK}}(\mathcal{G}, \mathcal{G}') = \langle \mathbf{f}_\mathcal{G}, \mathbf{f}_{\mathcal{G}'} \rangle, \quad (\text{S30})$$

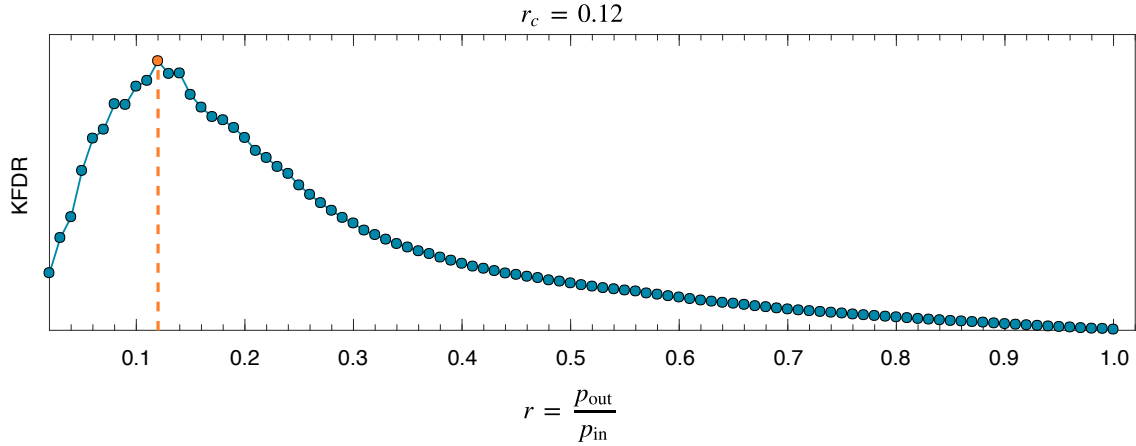
where  $\langle \cdot, \cdot \rangle$  represents the Euclidean dot product. In our experiments, we set  $k = 4$  for MUTAG, BZR, DHFR and FRANKENSTEIN datasets and  $k = 3$  for the other datasets.

**Weisfeiler–Lehman kernel.** This kernel decomposes a graph into its subtree patterns and compares these patterns in two graphs. For an unlabeled graph  $\mathcal{G}$ , all vertices  $v$  of  $\mathcal{G}$  are initialized with label  $\phi(v) = 0$ . We iterate over each vertex  $v$  and its neighbour to create a multiset label as  $\phi^{(i)}(v)$  such that  $\phi^{(1)}(v) = \phi(v)$ , and  $\phi^{(i)}$  with  $i > 1$  is defined as  $\phi^{(i)}(v) = (\phi^{(i)}(v), \mathbf{Q}_v^{(i-1)})$ , where  $\mathbf{Q}_v^{(i-1)}$  is the sorted labels of  $v$ 's neighbours. To measure the similarity between graphs, we count the co-occurrences of the labels in both graphs for  $h$  iterations with the kernel defined as

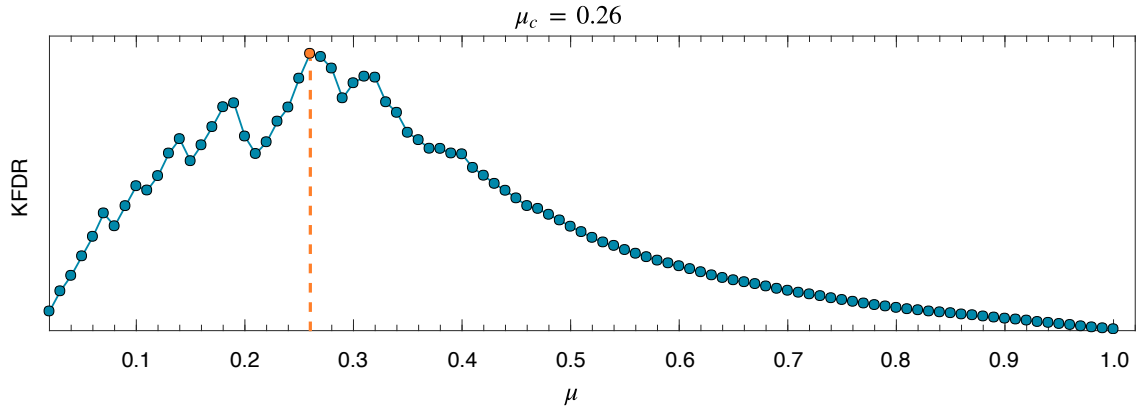
$$\mathcal{K}_{\text{WL}}(\mathcal{G}, \mathcal{G}') = \langle \mathbf{1}_\mathcal{G}, \mathbf{1}_{\mathcal{G}'} \rangle. \quad (\text{S31})$$

Here,  $\mathbf{1}_{\mathcal{G}}$  is the vector concatenation of  $h$  vertex label histograms  $\mathbf{1}_{\mathcal{G}}^{(1)}, \dots, \mathbf{1}_{\mathcal{G}}^{(h)}$  in  $h$  iterations. We set  $h = 5$  in our experiments.

## Supplementary Figures and Tables.



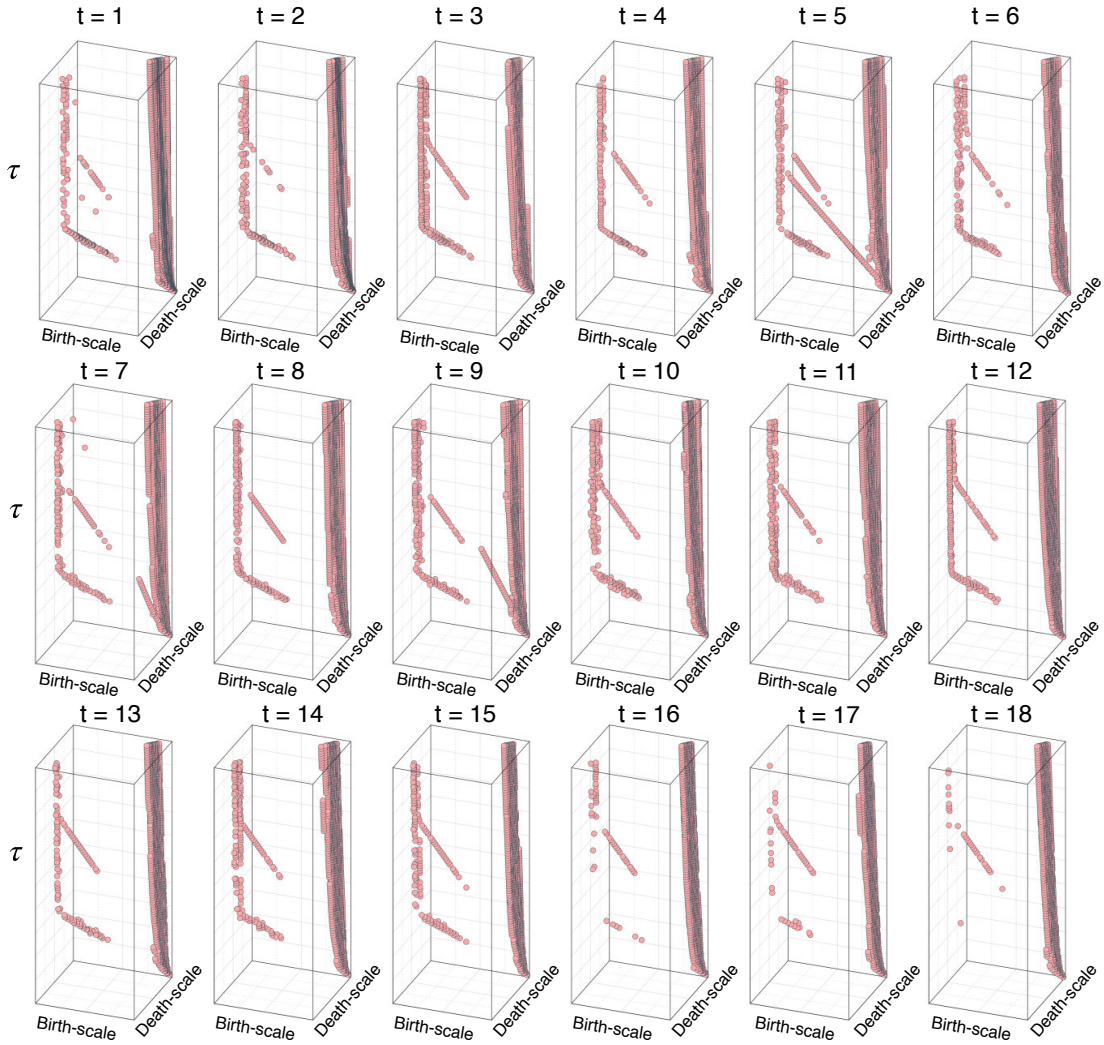
**Supplementary Figure 2 | Kernel Fisher discriminant ratio (KFDR) estimated for the series of Girvan–Newman networks.** We detect the transition point in the window of 100 persistence diagrams for one-dimensional holes obtained when increasing  $r = p_{\text{out}}/p_{\text{in}}$  as  $r_1 = 0.01, r_2 = 0.02, \dots, r_{100} = 1.0$ . The maximum value of KFDR is marked with the orange point. The transition point  $r_c = 0.12$  is the value of  $r$  that achieves the maximum KFDR.



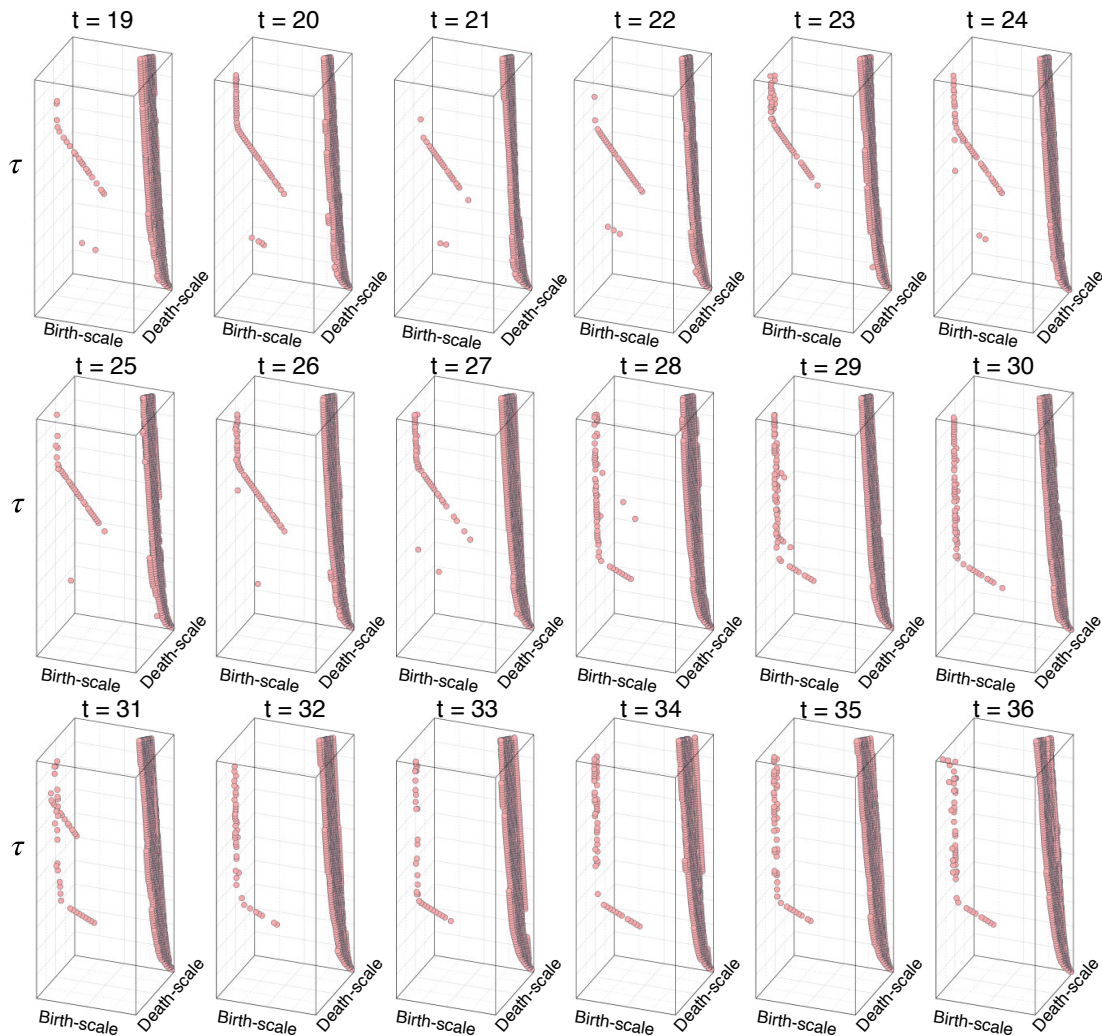
**Supplementary Figure 3 | Kernel Fisher discriminant ratio (KFDR) estimated for the series of Lancichinetti–Fortunato–Radicchi networks.** We detect the transition point in the window of 100 persistence diagrams for one-dimensional holes obtained when increasing  $\mu$  as  $\mu_1 = 0.01, \mu_2 = 0.02, \dots, \mu_{100} = 1.0$ . The maximum value of KFDR is marked with the orange point. The transition point  $\mu_c = 0.26$  is the value of  $\mu$  that achieves the maximum KFDR.

**Supplementary Table 1 | Summary statistics of the real-world network data.**

Dataset	Number of networks	Number of classes	Number of networks in each class	Average number of nodes	Average number of edges
MUTAG	188	2	(63,125)	17.93	19.79
BZR	405	2	(319, 86)	35.75	38.36
COX2	467	2	(365, 102)	41.22	43.45
DHFR	756	2	(295, 461)	42.43	44.54
FRANKENSTEIN	4337	2	(2401, 1936)	16.90	17.88
PROTEINS	1113	2	(663, 450)	39.06	72.82
NCI1	4110	2	(2053, 2057)	29.87	32.30
NCI109	4127	2	(2048, 2079)	29.68	32.13
IMDB–BINARY	1000	2	(500, 500)	19.77	96.53
IMDB–MULTI	1500	3	(500, 500, 500)	13.00	65.94

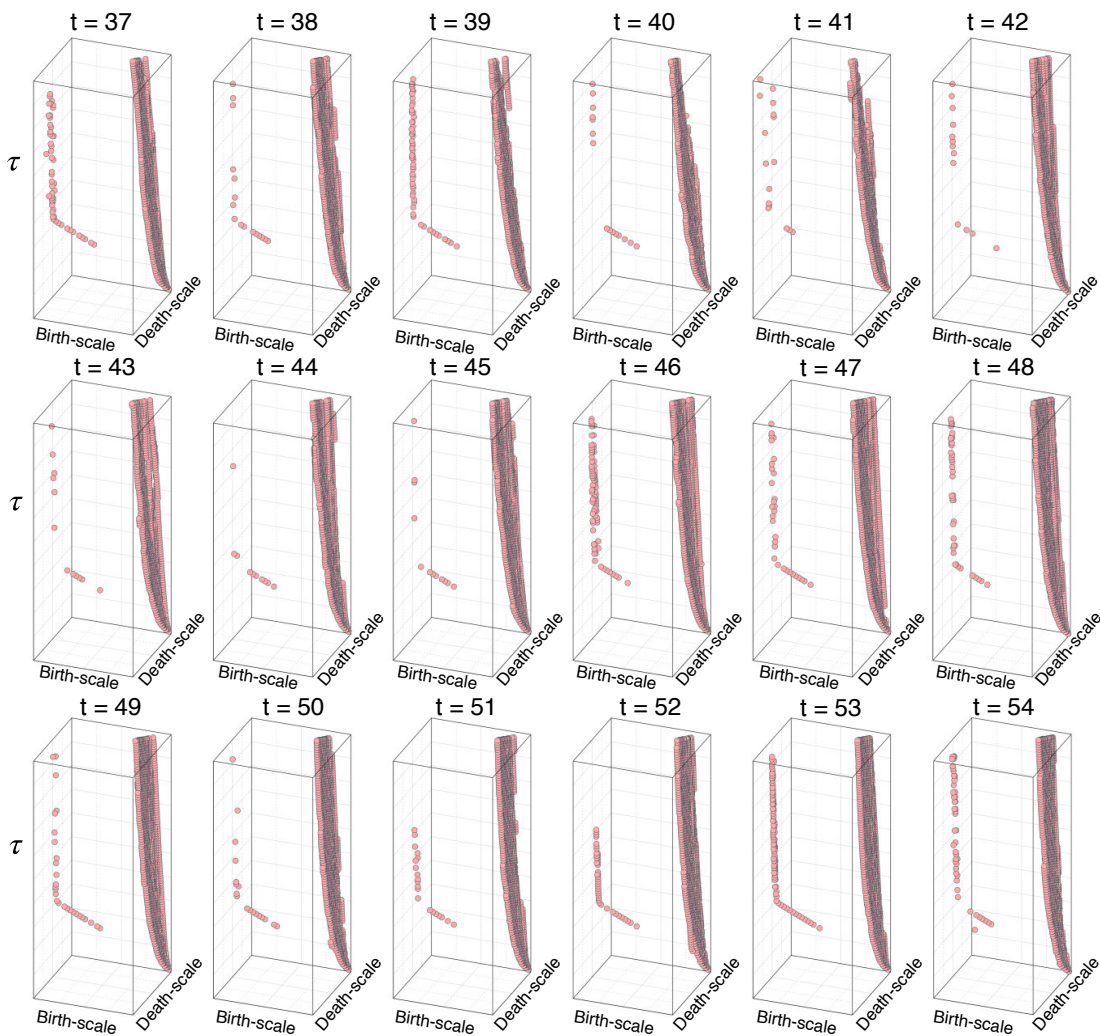


**Supplementary Figure 4 | Three-dimensional persistence diagrams of one-dimensional holes for the *Drosophila Melanogaster* gene regulatory networks spanning from  $t = 1$  to  $t = 18$ .** For each network at each time point, we compute three-dimensional persistence diagrams with timescale values  $\tau_1 = 1, \tau_2 = 2, \dots, \tau_{100} = 100$ . The birth-scale and the death-scale axes of the diagrams are represented at the logarithmic scale.

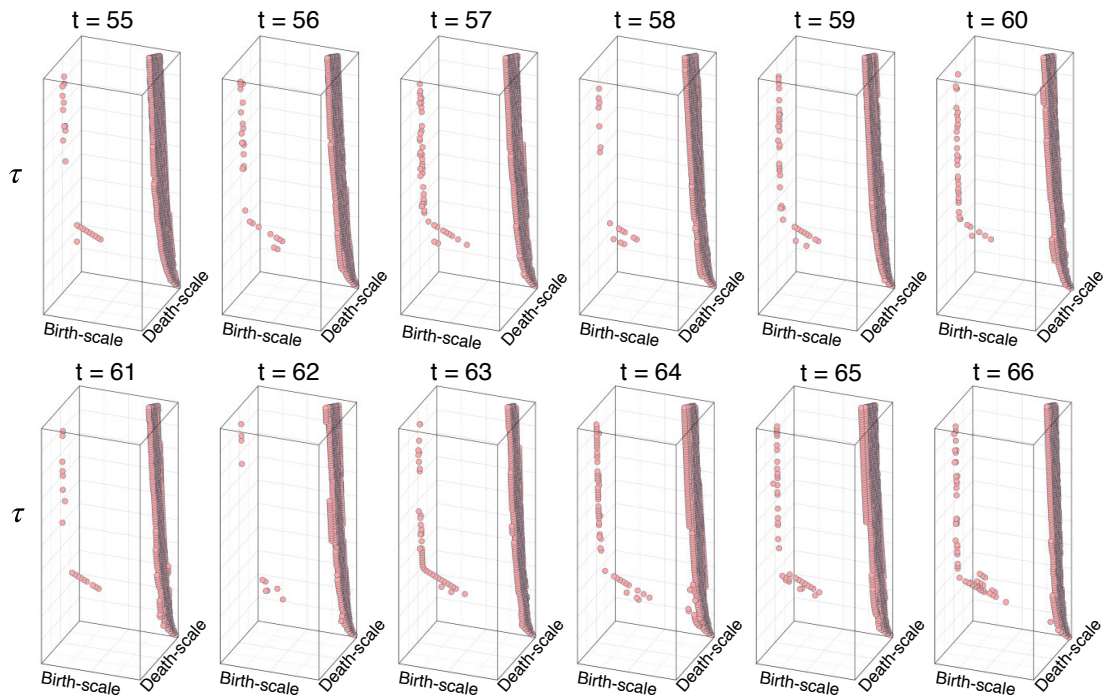


**Supplementary Figure 5 | Three-dimensional persistence diagrams of one-dimensional holes for the *Drosophila Melanogaster* gene regulatory networks spanning from  $t = 19$  to  $t = 36$ .** For each network at each time point, we compute three-dimensional persistence diagrams with timescale values  $\tau_1 = 1, \tau_2 = 2, \dots, \tau_{100} = 100$ . The birth-scale and the death-scale axes of the diagrams are represented at the logarithmic scale.





**Supplementary Figure 6 | Three-dimensional persistence diagrams of one-dimensional holes for the *Drosophila Melanogaster* gene regulatory networks spanning from  $t = 37$  to  $t = 54$ .** For each network at each time point, we compute three-dimensional persistence diagrams with timescale values  $\tau_1 = 1, \tau_2 = 2, \dots, \tau_{100} = 100$ . The birth-scale and the death-scale axes of the diagrams are represented at the logarithmic scale.



**Supplementary Figure 7 | Three-dimensional persistence diagrams of one-dimensional holes for the *Drosophila Melanogaster* gene regulatory networks spanning from  $t = 55$  to  $t = 66$ .** For each network at each time point, we compute three-dimensional persistence diagrams with timescale values  $\tau_1 = 1, \tau_2 = 2, \dots, \tau_{100} = 100$ . The birth-scale and the death-scale axes of the diagrams are represented at the logarithmic scale.

## References

1. Chazal, F., de Silva, V. & Oudot, S. Persistence stability for geometric complexes. *Geometriae Dedicata* **173**, 193–214 (2014).
2. Golub, G. H. & Van Loan, C. F. *Matrix computations*, vol. 3 (JHU Press, 2012).
3. Harchaoui, Z., Moulines, E. & Bach, F. R. Kernel change-point analysis. In *Adv. Neural Inf. Process. Syst.*, 609–616 (2009).
4. Kashima, H., Tsuda, K. & Inokuchi, A. Marginalized kernels between labeled graphs. In *Proceedings of the 20th International Conference on Machine Learning*, 321–328 (2003).
5. Gärtner, T., Flach, P. & Wrobel, S. On graph kernels: Hardness results and efficient alternatives. In *Proceedings of the 16th Annual Conference on Computational Learning Theory*, 129–143 (2003).
6. Borgwardt, K. M. & Kriegel, H.-P. Shortest-path kernels on graphs. In *Proceedings of the 5th IEEE International Conference on Data Mining*, 74–81 (2005).
7. Borgwardt, K. M., Petri, T., Vishwanathan, S. & Kriegel, H.-P. An efficient sampling scheme for comparison of large graphs. *MLG* (2007).
8. Shervashidze, N., Schweitzer, P., Leeuwen, E. J. v., Mehlhorn, K. & Borgwardt, K. M. Weisfeiler–Lehman graph kernels. *JMLR* **12**, 2539–2561 (2011).
9. Sugiyama, M., Ghisu, M. E., Llinares-López, F. & Borgwardt, K. graphkernels: R and python packages for graph comparison. *Bioinformatics* **34**, 530–532 (2017).